Editors' Suggestion

Prospects for geoneutrino detection with JUNO*

Thomas Adam[44] Shakeel Ahmad[65] Rizwan Ahmed[65] Fengpeng An (安丰鹏)[20]
João Pedro Athayde Marcondes de André[44] Costas Andreopoulos[74] Giuseppe Andronico[55] Nikolay Anfimov[66]
Vito Antonelli[59] Tatiana Antoshkina[66] Didier Auguste[47] Marcel Büchner[53] Weidong Bai (白伟东)[20]
Nikita Balashov[66] Andrea Barresi[58] Davide Basilico[59] Eric Baussan[44] Marco Beretta[59] Antonio Bergnoli[61]
Nikita Bessonov[66] Daniel Bick[50] Lukas Bieger[54] Svetlana Biktemerova[66] Thilo Birkenfeld[48] Simon Blyth[10]
Manuel Boehles[53] Anastasia Bolshakova[66] Mathieu Bongrand[46] Matteo Borghesi[58] Dominique Breton[47]
Augusto Brigatti[59] Riccardo Brugnera[60] Riccardo Bruno[55] Antonio Budano[63] Jose Busto[45] Anatael Cabrera[47]
Barbara Caccianiga[59] Hao Cai (蔡浩)[32] Xiao Cai (蔡啸)[10] Stéphane Callier[43] Steven Calvez[46] Antonio Cammi[57]
Guofu Cao (曹国富)[10] Jun Cao (曹俊)[10] Yaoqi Cao[73,74] Rossella Caruso[55] Cédric Cerna[43] Vanessa Cerrone[60]
Jinfan Chang (常劲帆)[10] Yun Chang (张昀)[38] Tim Charisse[49,53] Auttakit Chatrabhuti[70] Chao Chen (陈超)[10]
Haotian Chen (陈浩天)[10] Jiahui Chen (陈家会)[10] Jian Chen (陈建)[20] Jing Chen (陈静)[20] Junyou Chen (陈俊有)[26]
Pingping Chen (陈平平)[17] Shaomin Chen (陈少敏)[12] Shiqiang Chen (陈士强)[25] Yixue Chen (陈义学)[11]
Yu Chen (陈羽)[20] Ze Chen[49,53] Zhangming Chen (陈张铭)[28] Zhiyuan Chen (陈志源)[10,18]
Zhongchang Chen (陈忠昌)[77] Jie Cheng (程捷)[11] Yaping Cheng (程雅苹)[7] Yu Chin Cheng (鄭宇晉)[39]
Alexander Chepurnov[68,67] Alexey Chetverikov[66] Davide Chiesa[58] Pietro Chimenti[3] Po-Lin Chou (周伯麟)[36]
Ziliang Chu (褚子良)[10] Artem Chukanov[66] Gérard Claverie[43] Catia Clementi[62] Barbara Clerbaux[2] Claudio Coletta[58]
Marta Colomer Molla[2] Chenyang Cui (崔晨阳)[10] Ziyan Deng (邓子艳)[10] Xiaoyu Ding (丁晓雨)[27]
Xuefeng Ding (丁雪峰)[10] Yayun Ding (丁雅韵)[10] Bayu Dirgantara[72] Sergey Dmitrievsky[66] Dmitry Dolzhikov[66]
Chuanshi Dong (董川石)[10] Haojie Dong (董灏杰)[10] Jianmeng Dong (董建蒙)[12] Evgeny Doroshkevich[67]
Marcos Dracos[44] Frédéric Druillole[43] Ran Du (杜然)[10] Shuxian Du (杜书先)[35] Katherine Dugas[75] Stefano Dusini[61]
Hongyue Duyang (杜杨洪岳)[27] Jessica Eck[54] Andrea Fabbri[63] Ulrike Fahrendholz[52] Lei Fan (樊磊)[10]
Liangqianjin Fan (范良前进)[10] Jian Fang (方建)[10] Wenxing Fang (方文兴)[10] Elia Stanescu Farilla[63]
Dmitry Fedoseev[66] Li-Cheng Feng (馮立誠)[36] Qichun Feng (冯启春)[21] Shaoting Feng (冯绍庭)[77] Daniela Fetzer[53]
Marcellin Fotzé[44] Amélie Fournier[43] Aaron Freegard[28] Ying Fu (付颖)[10,18] Haonan Gan (甘浩男)[30]
Feng Gao (高峰)[2] Ruohan Gao (高若菡)[8] Alberto Garfagnini[60] Arsenii Gavrikov[60] Marco Giammarchi[59]
Nunzio Giudice[55] Maxim Gonchar[66] Guanda Gong (宫冠达)[10,18] Guanghua Gong (龚光华)[12] Yuri Gornushkin[66]
Marco Grassi (马酷)[60] Maxim Gromov[68,66] Vasily Gromov[66] Minhao Gu (顾旻皓)[10] Xiaofei Gu (谷肖飞)[35]
Yu Gu (古宇)[19] Mengyun Guan (关梦云)[10] Yuduo Guan (管宇铎)[10] Nunzio Guardone[55] Rosa Maria Guizzetti[60]
Cong Guo (郭聪)[10] Wanlei Guo (郭万磊)[10] Caren Hagner[50] Hechong Han (韩鹤冲)[10] Ran Han (韩然)[11]
Yang Han (韩阳)[20] Chuanhui Hao (郝传晖)[12] Vidhya Thara Hariharan[50] Miao He (何苗)[10] Wei He (何伟)[10]

Received 24 November 2025; Accepted 11 February 2026; Accepted manuscript online 12 February 2026

* This work was supported in part by the Chinese Academy of Sciences, the National Key R&D Program of China, the Guangdong provincial government, and the Tsung-Dao Lee Institute of Shanghai Jiao Tong University in China, the Institut National de Physique Nucléaire et de Physique de Particules (IN2P3) in France, the Istituto Nazionale di Fisica Nucleare (INFN) in Italy, the Fond de la Recherche Scientifique (F.R.S\-FNRS) and the Institut Interuniversitaire des Sciences Nucléaires (IISN) in Belgium, the Conselho Nacional de Desenvolvimento Científico e Tecnológico in Brazil, the Agencia Nacional de Investigacion y Desarrollo and ANID - Millennium Science Initiative Program - ICN2019_044 in Chile, The European Structural and Investment Funds, the Czech Ministry of Education, Youth and Sports and the Charles University Research Centerin Czech Republic, Deutsche Forschungsgemeinschaft (DFG), the Helmholtz Association, and the Cluster of Excellence PRISMA+ in Germany, the Joint Institute of Nuclear Research (JINR) and Lomonosov Moscow State University in Russia, the Slovak Research and Development Agency in Slovakia, MOST and MOE in Taipei, the Program Management Unit for Human Resources & Institutional Development, Research and Innovation, Chulalongkorn University, and Suranaree University of Technology in Thailand, the Science and Technology Facilities Council (STFC) in the UK, University of California at Irvine and the National Science Foundation in the US.

Content from this work may be used under the terms of the Creative Commons Attribution 3.0 licence. Any further distribution of this work must maintain attribution to the author(s) and the title of the work, journal citation and DOI. Article funded by SCOAP[3] and published under licence by Chinese Physical Society and the Institute of High Energy Physics of the Chinese Academy of Sciences and the Institute of Modern Physics of the Chinese Academy of Sciences and IOP Publishing Ltd

Xinhai He (贺新海)[10] Ziou He[73,74] Tobias Heinz[54] Patrick Hellmuth[43] Yuekun Heng (衡月昆)[10]
YuenKeung Hor (贺远强)[20] Shaojing Hou (侯少静)[10] Fatima Houria[59] Yee Hsiung (熊怡)[39] Bei-Zhen Hu (胡贝祯)[40]
Hang Hu (胡航)[20] Jun Hu (胡俊)[10] Tao Hu (胡涛)[10] Yuxiang Hu (胡宇翔)[10] Guihong Huang (黄桂鸿)[23]
Jinhao Huang (黄金浩)[10] Junlin Huang (黄俊霖)[19] Junting Huang (黄俊挺)[28] Kaixuan Huang (黄凯旋)[20]
Shengheng Huang (黄生恒)[23] Tao Huang (黄涛)[20] Xin Huang (黄鑫)[10] Xingtao Huang (黄性涛)[27]
Yongbo Huang (黄永波)[26] Jiaqi Hui (惠加琪)[28] Lei Huo (霍雷)[21] Cédric Huss[43] Safeer Hussain[65] Leonard Imbert[46]
Ara Ioannisian[1] Adrienne Jacobi[75] Arshak Jafar[53] Beatrice Jelmini[60] Xiangpan Ji (季向盼)[31] Xiaolu Ji (季筱璐)[10]
Junji Jia (贾俊基)[32] Cailian Jiang (江彩莲)[25] Guangzheng Jiang (姜光政)[15] Junjie Jiang[28] Xiaoshan Jiang (江晓山)[10]
Xiaozhao Jiang (江晓照)[10] Yijian Jiang (姜轶剑)[11] Yixuan Jiang (蒋奕萱)[10] Xiaoping Jing (荆小平)[10]
Cécile Jollet[43] Liam Jones[73,74] Li Kang (康丽)[17] Narine Kazarian[1] Ali Khan[65] Amina Khatun[2,69]
Khanchai Khosonthongkee[72] Denis Korablev[66] Konstantin Kouzakov[68] Alexey Krasnoperov[66] Sergey Kuleshov[5]
Sindhujha Kumaran[75] Nikolay Kutovskiy[66] Loïc Labit[43] Tobias Lachenmaier[54] Haojing Lai (赖浩菁)[28]
Cecilia Landini[59] Lorenzo Lastrucci[60] Sébastien Leblanc[43] Matthieu Lecocq[43] Frederic Lefevre[46]
Ruiting Lei (雷瑞庭)[17] Rupert Leitner[41] Petr Lenskii[66] Jason Leung[36] Demin Li (李德民)[35] Fei Li (李飞)[10]
Gaosong Li (李高嵩)[10] Jiajun Li (李佳俊)[20] Meiou Li (李美鸥)[23] Min Li (李民)[44] Nan Li (李楠)[14]
Ruhui Li (李茹慧)[10] Rui Li (李瑞)[28] Shanfeng Li (黎山峰)[17] Teng Li (李腾)[27] Weidong Li (李卫东)[10,13]
Xiaonan Li (李小男)[18] Yi Li (李仪)[17] Yichen Li (李依宸)[10] Yifan Li (李一帆)[10] Yingke Li (李应可)[26]
Yufeng Li (李玉峰)[10] Zhaohan Li (李兆涵)[10] Zhibing Li (李志兵)[20] Zhiwei Li (李志伟)[8] Zi-Ming Li[35]
An-An Liang[36] Jiajun Liao (廖佳军)[20] Minghua Liao (廖明华)[20] Yilin Liao (廖依林)[28] Ayut Limphirat[72]
Bo-Chun Lin[36] Guey-Lin Lin (林貴林)[36] Shengxin Lin (林盛鑫)[17] Tao Lin (林韬)[10] Xingyi Lin (林兴毅)[26]
Jiajie Ling (凌家杰)[20] Xin Ling (凌鑫)[10] Ivano Lippi[61] Caimei Liu (刘彩美)[10] Fang Liu (刘芳)[11]
Fengcheng Liu (刘峰成)[11] Haidong Liu (刘海东)[35] Hongbang Liu (刘宏邦)[26] Hongjuan Liu (刘红娟)[22]
Jianglai Liu (刘江来)[28,29] Jiaxi Liu (刘佳熙)[10] Jinchang Liu (刘金昌)[10] Kainan Liu (刘凯楠)[23] Min Liu (刘敏)[22]
Qian Liu (刘倩)[13] Runxuan Liu (刘润轩)[49,48] Shenghui Liu (刘生辉)[10] Shulin Liu (刘术林)[10] Ximing Liu (刘希明)[31]
Xiwen Liu (刘熙文)[26] Xuewei Liu (刘学伟)[12] Yankai Liu (刘颜恺)[33] Yiqi Liu (刘逸祺)[12] Zhipeng Liu (刘志鹏)[10]
Zhuo Liu (刘卓)[10] Lorenzo Loi[57] Alexey Lokhov[67,68] Paolo Lombardi[59] Kai Loo[42] Selma Conforti Di Lorenzo[43]
Chuan Lu (陆川)[30] Haoqi Lu (路浩奇)[10] Junguang Lu (吕军光)[10] Meishu Lu[52] Shuxiang Lu (路书祥)[35]
Xianguo Lu[73] Bayarto Lubsandorzhiev[67] Sultim Lubsandorzhiev[67] Livia Ludhova[49,53] Arslan Lukanov[67]
Fengjiao Luo (罗凤蛟)[22] Guang Luo (罗光)[20] Jianyi Luo (罗坚义)[20] Shu Luo (罗舒)[34] Wuming Luo (罗武鸣)[10]
Xiaojie Luo (罗晓杰)[10] Vladimir Lyashuk[67] Bangzheng Ma (马帮争)[27] Bing Ma (马冰)[35] Qiumei Ma (马秋梅)[10]
Si Ma (马斯)[10] Wing Yan Ma (马咏恩)[27] Xiaoyan Ma (马骁妍)[10] Xubo Ma (马续波)[11] Jihane Maalmi[47]
Jingyu Mai (麦景宇)[20] Marco Malabarba[49,53] Yury Malyshkin[49,53] Roberto Carlos Mandujano[75] Fabio Mantovani[56]
Xin Mao (冒鑫)[7] Stefano M. Mari[63] Agnese Martini[64] Johann Martyn[53] Matthias Mayer[52] Davit Mayilyan[1]
William McDonough[76] Yue Meng (孟月)[28] Anselmo Meregaglia[43] Lino Miramonti[59] Michele Montuschi[56]
Iwan Morton-Blake[29] Xiangyi Mu (牟向翊)[10] Massimiliano Nastasi[58] Dmitry V. Naumov[66] Elena Naumova[66]
Igor Nemchenok[66] Elisabeth Neuerburg[48] Alexey Nikolaev[68] Feipeng Ning (宁飞鹏)[10] Zhe Ning (宁哲)[10]
Yujie Niu (牛玉杰)[10] Hiroshi Nunokawa[4] Lothar Oberauer[52] Juan Pedro Ochoa-Ricoux[5,75] Sebastian Olivares[6]
Alexander Olshevskiy[66] Domizia Orestano[63] Fausto Ortica[62] Rainer Othegraven[53] Yifei Pan (潘一飞)[20]
Alessandro Paoloni[64] George Parker[53] Yatian Pei (裴亚田)[10] Luca Pelicci[59] Anguo Peng (彭安国)[22]
Yu Peng (彭宇)[10] Zhaoyuan Peng (彭昭缘)[10] Elisa Percalli[59] Willy Perrin[44] Frédéric Perrot[43]
Pierre-Alexandre Petitjean[2] Fabrizio Petrucci[63] Oliver Pilarczyk[53] Artyom Popov[68] Pascal Poussot[44] Ezio Previtali[58]
Fazhi Qi (齐法制)[10] Ming Qi (祁鸣)[25] Sen Qian (钱森)[10] Xiaohui Qian (钱小辉)[10] Zhonghua Qin (秦中华)[10]
Shoukang Qiu (丘寿康)[22] Manhao Qu (屈满昊)[35] Zhenning Qu (曲振宁)[10] Gioacchino Ranucci[59]
Thomas Raymond[44] Alessandra Re[59] Abdel Rebii[43] Mariia Redchuk[61] Bin Ren (任斌)[17] Yuhan Ren (任雨涵)[10]
Cristobal Morales Reveco[49,48,53] Barbara Ricci[56] Mariam Rifai[49,48,53] Mathieu Roche[43] Narongkiat Rodphai[10]
Fernanda de Faria Rodrigues[10] Aldo Romani[62] Bedřich Roskovec[41] Peter Rudakov[68] Arseniy Rybnikov[66]

Andrey Sadovsky[66] Deshan Sandanayake[44] Anut Sangka[71] Ujwal Santhosh[49,53] Utane Sawangwit[71]
Michaela Schever[48] Cédric Schwab[44] Konstantin Schweizer[52] Alexandr Selyunin[66] Andrea Serafini[61]
Mariangela Settimo[46] Yanjun Shang (尚彦军)[9] Junyu Shao (邵俊禹)[10] Anurag Sharma[54] Vladislav Sharov[66]
Hangyu Shi (石航宇)[20] Hexi SHI[63] Jingyan Shi (石京燕)[10] Yuan Shi (石源)[10] Yike Shu (舒以科)[10]
Yuhan Shu (舒宇涵)[10] She Shuai (佘帅)[35] Vitaly Shutov[66] Andrey Sidorenkov[67] Fedor Šimkovic[69]
Randhir Singh[10,18] Apeksha Singhal[49] Chiara Sirignano[60] Jaruchit Siripak[72] Monica Sisti[58] Mikhail Smirnov[50]
Oleg Smirnov[66] Thiago Sogo-Bezerra[46] Sergey Sokolov[66] Julanan Songwadhana[72] Albert Sotnikov[66]
Warintorn Sreethawong[72] Achim Stahl[48] Luca Stanco[61] Konstantin Stankevich[68] Hans Steiger[52,53]
Jochen Steinmann[48] Tobias Sterr[54] Matthias Raphael Stock[52] Virginia Strati[56] Mikhail Strizh[68,67]
Alexander Studenikin[68] Aoqi Su (苏奥琪)[35] Jun Su (苏军)[20] Guangbao Sun (孙光豹)[32] Mingxia Sun (孙明霞)[10]
Xilei Sun (孙希磊)[10] Yongzhao Sun (孙永昭)[10] Zhanxue Sun (孙占学)[24] Zhengyang Sun (孙正阳)[29]
Narumon Suwonjandee[70] Christophe De La Taille[43] Akira Takenaka[20] Xiaohan Tan (谭晓晗)[27]
Haozhong Tang (唐淏忠)[10] Jian Tang (唐健)[20] Jingzhe Tang (唐经哲)[26] Quan Tang (唐泉)[22] Xiao Tang (唐晓)[10]
Jihua Tao (陶继华)[24] Minh Thuan Nguyen Thi[36] Yuxin Tian (田雨欣)[29] Igor Tkachev[67] Tomas Tmej[41]
Marco Danilo Claudio Torri[59] Andrea Triossi[60] Wladyslaw Trzaska[42] Andrei Tsaregorodtsev[45] Yu-Chen Tung[37]
Cristina Tuve[55] Nikita Ushakov[67] Carlo Venettacci[63] Giuseppe Verde[55] Maxim Vialkov[68] Benoit Viaud[46]
Cornelius Moritz Vollbrecht[49,48] Vit Vorobel[41] Dmitriy Voronin[67] Lucia Votano[64] Andong Wang (王安东)[24]
Caishen Wang (王彩申)[17] Chung-Hsiang Wang (王正祥)[38] En Wang (王恩)[35] Hanwen Wang (王翰文)[10]
Jiabin Wang (王家斌)[27] Jun Wang (王俊)[20] Ke Wang (王科)[77] Li Wang (王莉)[10,35] Meng Wang (王孟)[22]
Meng Wang (王孟)[27] Mingyuan Wang (王明远)[10] Ruiguang Wang (王瑞光)[10]
Sibo Wang (王思博)[10] Tianhong Wang (王天鸿)[21] Wei Wang (王为)[20] Wenshuai Wang (王文帅)[10] Wenyuan Wang[27]
Xi Wang (王玺)[14] Yangfu Wang (王仰夫)[10] Yaoguang Wang (王耀光)[27] Yi Wang (王忆)[10]
Yifang Wang (王贻芳)[10] Yuyi Wang (王宇逸)[12] Zhe Wang (王喆)[12] Zheng Wang (王铮)[10] Zhimin Wang (王志民)[10]
Apimook Watcharangkool[71] Junya Wei (魏俊雅)[27] Jushang Wei (魏居尚)[27] Wei Wei (魏巍)[10] Wei Wei (魏巍)[27]
Yadong Wei (魏亚东)[17] Yuehuan Wei (魏月环)[20] Zhengbao Wei (韦正宝)[26] Liangjian Wen (温良剑)[10]
Jun Weng (翁俊)[12] Scott Wipperfurth[76] Rosmarie Wirth[49,53] Bi Wu (吴比)[20] Chengxin Wu (吴城鑫)[20]
Qun Wu (吴群)[27] Yinhui Wu (吴寅慧)[10] Zhaoxiang Wu (吴肇祥)[10] Zhi Wu (吴智)[10] Michael Wurm[53]
Jacques Wurtz[44] Yufei Xi (习宇飞)[30] Dongmei Xia (夏冬梅)[16] Shishen Xian (咸世莘)[29] Ziqian Xiang (向子谦)[28]
Fei Xiao (肖菲)[10] Pengfei Xiao (肖鹏飞)[10] Tianying Xiao (肖天颖)[26] Xiang Xiao[20] Wei-Jun Xie[36]
Xiaochuan Xie (谢小川)[26] Yuguang Xie (谢宇广)[10] Zhao Xin (辛钊)[10] Zhizhong Xing (邢志忠)[10]
Benda Xu (续本达)[12] Cheng Xu (徐程)[22] Chuang Xu (徐闯)[12] Donglian Xu (徐东莲)[28,29] Fanrong Xu (徐繁荣)[19]
Jiayang Xu (徐嘉洋)[10] Jie Xu (徐杰)[8] Jilei Xu (徐吉磊)[10] Jinghuan Xu (徐靖桓)[26] Meihang Xu (徐美杭)[10]
Shiwen Xu (许释文)[10] Xunjie Xu (许勋杰)[10] Ya Xu (徐亚)[9] Dongyang Xue (薛东阳)[12] Jingqin Xue (薛景秦)[10]
Baojun Yan (闫保军)[10] Qiyu Yan (严启宇)[13,73] Taylor Yan[72] Xiongbo Yan (严雄波)[10] Yupeng Yan[72]
Changgen Yang (杨长根)[10] Chengfeng Yang (杨成峰)[20] Dikun Yang (杨迪琨)[77] Fengfan Yang (杨冯帆)[10]
Jie Yang (杨洁)[35] Kaiwei Yang (杨开为)[10] Lei Yang (杨雷)[17] Pengfei Yang (杨鹏飞)[20] Xiaoyu Yang (杨晓宇)[10]
Xuhui Yang (杨旭晖)[10] Yifan Yang (杨翊凡)[2] Zekun Yang (杨泽坤)[27] Haifeng Yao (姚海峰)[10]
Jiaxaun Ye (叶佳璇)[10] Mei Ye (叶梅)[10] Ziping Ye (叶子平)[29] Frédéric Yermia[46] Jilong Yin (尹纪龙)[10]
Weiqing Yin (尹维卿)[10] Xiaohao Yin (尹小豪)[20] Zhengyun You (尤郑昀)[20] Boxiang Yu (俞伯祥)[10]
Chiye Yu (余炽业)[17] Chunxu Yu (喻纯旭)[31] Hongzhao Yu (余泓钊)[10,18] Peidong Yu (于佩东)[10] Simi Yu (禹思蜜)[23]
Zeyuan Yu (于泽源)[10] Cenxi Yuan (袁岑溪)[20] Noman Zafar[65] Jilberto Zamora[6] Vitalii Zavadskyi[66]
Fanrui Zeng (曾凡蕊)[27] Shan Zeng (曾珊)[10] Tingxuan Zeng (曾婷轩)[10] Liang Zhan (占亮)[10] Bin Zhang (张斌)[35]
Feiyang Zhang (张飞洋)[28] Han Zhang (张涵)[10] Hangchang Zhang (张航畅)[10] Haosen Zhang (张豪森)[10]
Honghao Zhang (张宏浩)[20] Jialiang Zhang (张家梁)[25] Jiawen Zhang (张家文)[10] Jie Zhang (张杰)[10]
Jingbo Zhang (张景波)[21] Junwei Zhang (张峻玮)[26] Lei Zhang (张雷)[25] Ping Zhang (张平)[28]
Qingmin Zhang (张清民)[33] Rongping Zhang (张荣凭)[10] Shiqi Zhang (张石其)[20] Shuihan Zhang (张水涵)[10]

Siyuan Zhang (张思远)[26] Tao Zhang (张涛)[28] Xiaomei Zhang (张晓梅)[10] Xu Zhang (张叙)[10]
Xuantong Zhang (张玄同)[10] Yibing Zhang (张依兵)[10,18] Yinhong Zhang (张银鸿)[10] Yiyu Zhang (张易于)[10]
Yongpeng Zhang (张永鹏)[10] Yuanyuan Zhang (张圆圆)[29] Yue Zhang (张越)[27] Yumei Zhang (张玉美)[20]
Zhenyu Zhang (张振宇)[32] Zhicheng Zhang (张志诚)[27] Zhijian Zhang (张志坚)[17] Jie Zhao (赵洁)[10]
Liang Zhao (赵亮)[9] Runze Zhao (赵润泽)[10,18] Shujun Zhao (赵书俊)[35] Hua Zheng (郑华)[17]
Yangheng Zheng (郑阳恒)[13] Li Zhou (周莉)[10] Lishui Zhou (周丽水)[77] Shun Zhou (周顺)[10] Xiang Zhou (周详)[32]
Xing Zhou (周星)[10] Jingsen Zhu (朱景森)[20] Kangfu Zhu (朱康甫)[33] Kejun Zhu (朱科军)[10] Bo Zhuang (庄博)[10]
Honglin Zhuang (庄红林)[10] Ivan Zhutikov[66] Jiaheng Zou (邹佳恒)[10]
(JUNO Collaboration)

[1]Yerevan Physics Institute, Yerevan, Armenia
[2]Université Libre de Bruxelles, Brussels, Belgium
[3]Universidade Estadual de Londrina, Londrina, Brazil
[4]Pontificia Universidade Catolica do Rio de Janeiro, Rio de Janeiro, Brazil
[5]Millennium Institute for SubAtomic Physics at the High-energy Frontier (SAPHIR), ANID, Chile
[6]Universidad Andres Bello, Fernandez Concha 700, Chile
[7]Beijing Institute of Spacecraft Environment Engineering, Beijing, China
[8]China University of Geosciences, Beijing, China
[9]Insititute of Geology and Geophysics, Chinese Academy of Sciences, Beijing, China
[10]Institute of High Energy Physics, Beijing, China
[11]North China Electric Power University, Beijing, China
[12]Tsinghua University, Beijing, China
[13]University of Chinese Academy of Sciences, Beijing, China
[14]College of Electronic Science and Engineering, National University of Defense Technology, Changsha, China
[15]Chengdu University of Technology, Chengdu, China
[16]Chongqing University, Chongqing, China
[17]Dongguan University of Technology, Dongguan, China
[18]Kaiping Neutrino Research Center, Guangdong, China
[19]Jinan University, Guangzhou, China
[20]Sun Yat-Sen University, Guangzhou, China
[21]Harbin Institute of Technology, Harbin, China
[22]University of South China, Hengyang, China
[23]Wuyi University, Jiangmen, China
[24]East China University of Technology, Nanchang, China
[25]Nanjing University, Nanjing, China
[26]Guangxi University, Nanning, China
[27]Shandong University, Jinan, China, and Key Laboratory of Particle Physics and Particle Irradiation of Ministry of Education, Shandong University, Qingdao, China
[28]School of Physics and Astronomy, Shanghai Jiao Tong University, Shanghai, China
[29]Tsung-Dao Lee Institute, Shanghai Jiao Tong University, Shanghai, China
[30]Institute of Hydrogeology and Environmental Geology, Chinese Academy of Geological Sciences, Shijiazhuang, China
[31]Nankai University, Tianjin, China
[32]Wuhan University, Wuhan, China
[33]Xi'an Jiaotong University, Xi'an, China
[34]Xiamen University, Xiamen, China
[35]School of Physics and Microelectronics, Zhengzhou University, Zhengzhou, China
[36]Institute of Physics, National Yang Ming Chiao Tung University, Hsinchu
[37]Department of Physics, National Kaohsiung Normal University, Kaohsiung
[38]National United University, Miao-Li
[39]Department of Physics, National Taiwan University, Taipei
[40]Department of Electro-Optical Engineering, National Taipei University of Technology, Taipei
[41]Charles University, Faculty of Mathematics and Physics, Prague, Czech Republic
[42]University of Jyvaskyla, Department of Physics, Jyvaskyla, Finland
[43]Univ. Bordeaux, CNRS, LP2I, UMR 5797, F-33170 Gradignan, F-33170 Gradignan, France
[44]IPHC, Université de Strasbourg, CNRS/IN2P3, F-67037 Strasbourg, France
[45]Aix Marseille Univ, CNRS/IN2P3, CPPM, Marseille, France
[46]Nantes Université, IMT Atlantique, CNRS/IN2P3, Nantes, France
[47]IJCLab, Université Paris-Saclay, CNRS/IN2P3, 91405 Orsay, France
[48]III. Physikalisches Institut B, RWTH Aachen University, Aachen, Germany
[49]GSI Helmholtzzentrum für Schwerionenforschung GmbH, Planckstr. 1, 64291 Darmstadt, German
[50]Institute of Experimental Physics, University of Hamburg, Hamburg, Germany
[51]Forschungszentrum Jülich GmbH, Nuclear Physics Institute IKP-2, Jülich, Germany
[52]Technische Universität München, München, Germany
[53]Institute of Physics and EC PRISMA$^+$, Johannes Gutenberg Universität Mainz, Mainz, Germany
[54]Eberhard Karls Universität Tübingen, Physikalisches Institut, Tübingen, Germany

[55]INFN Catania and Dipartimento di Fisica e Astronomia dell Università di Catania, Catania, Italy
[56]Department of Physics and Earth Science, University of Ferrara and INFN Sezione di Ferrara, Ferrara, Italy
[57]INFN Milano Bicocca and Politecnico of Milano, Milano, Italy
[58]INFN Milano Bicocca and University of Milano Bicocca, Milano, Italy
[59]INFN Sezione di Milano and Dipartimento di Fisica dell Università di Milano, Milano, Italy
[60]Dipartimento di Fisica e Astronomia dell'Università di Padova and INFN Sezione di Padova, Padova, Italy
[61]INFN Sezione di Padova, Padova, Italy
[62]INFN Sezione di Perugia and Dipartimento di Chimica, Biologia e Biotecnologie dell'Università di Perugia, Perugia, Italy
[63]Dipartimento di Matematica e Fisica, Università Roma Tre and INFN Sezione Roma Tre, Roma, Italy
[64]Laboratori Nazionali di Frascati dell'INFN, Roma, Italy
[65]Pakistan Institute of Nuclear Science and Technology, Islamabad, Pakistan
[66]Joint Institute for Nuclear Research, Dubna, Russia
[67]Institute for Nuclear Research of the Russian Academy of Sciences, Moscow, Russia
[68]Lomonosov Moscow State University, Moscow, Russia
[69]Comenius University Bratislava, Faculty of Mathematics, Physics and Informatics, Bratislava, Slovakia
[70]High Energy Physics Research Unit, Faculty of Science, Chulalongkorn University, Bangkok, Thailand
[71]National Astronomical Research Institute of Thailand, Chiang Mai, Thailand
[72]Suranaree University of Technology, Nakhon Ratchasima, Thailand
[73]University of Warwick, University of Warwick, Coventry, CV4 7AL, United Kingdom
[74]The University of Liverpool, Department of Physics, Oliver Lodge Laboratory, Oxford Str., Liverpool L69 7ZE, United Kingdom
[75]Department of Physics and Astronomy, University of California, Irvine, California, USA
[76]Department of Geology, University of Maryland, College Park, USA
[77]Department of Earth and Space Sciences, Southern University of Science and Technology, Shenzhen, China

Abstract: Geoneutrinos—antineutrinos emitted during the decay of long-lived radioactive elements inside the Earth—serve as a unique tool for studying our planet's composition and heat budget. The Jiangmen Underground Neutrino Observatory (JUNO) experiment in China, which has recently completed construction, is expected to collect a sample comparable in size to the entire existing world geoneutrino dataset in less than a year. This paper presents an updated estimation of JUNO's sensitivity to geoneutrinos using the best knowledge available to date about the experimental site, the surrounding nuclear reactors, the detector response uncertainties, and the knowledge of the reactor antineutrino flux. To facilitate comparison with present and future geological models, our results cover a wide range of predicted signal strengths. Despite the significant background from reactor antineutrinos, the primary channel JUNO will use to determine the neutrino mass ordering, the experiment will measure the total geoneutrino flux with a precision comparable to that of existing experiments within its first few years, ultimately achieving a world-leading precision of about 8% over ten years. JUNO's large statistics will also allow separation of the Uranium-238 and Thorium-232 contributions with unprecedented precision, providing crucial constraints on models of Earth's formation and composition. Observation of the mantle signal above the lithospheric flux will be possible but challenging. For models with the highest predicted mantle concentrations of heat-producing elements, a ~3σ detection over six years requires knowledge of the lithospheric flux to within 15%. Together with complementary measurements from other locations, JUNO's geoneutrino results will offer cutting-edge, high-precision insights into the Earth's interior, of fundamental importance to both the geoscience and neutrino physics communities.

Keywords: geo-neutrino, JUNO, geo-science, sensitivity

DOI: 10.1088/1674-1137/ae457d **CSTR:** 32044.14.ChinesePhysicsC.50063003

I. INTRODUCTION

Geoneutrinos are electron antineutrinos ($\bar{\nu}_e$) originating from the radioactive decays of isotopes with half-lives comparable to or longer than Earth's age. These isotopes — ^{232}Th, ^{238}U, and ^{40}K—are naturally present inside the Earth and contribute to a total surface geoneutrino flux of nearly 10^7 cm^{-2} s^{-1} [28, 45]. Geoneutrinos represent a unique tool for tracing the total abundance, distribution and relative proportion of these so-called *Heat-Producing Elements* (HPEs) in the deep Earth. This knowledge provides insights into the Earth's radiogenic heat, a key parameter for geoscience, as well as into the dynamics of mantle convection, mantle homogeneity, and Earth's formation processes. Particularly intriguing is the question of the poorly known radiogenic heat from the Earth's mantle, as HPEs are primarily concentrated in the much better-known Earth's crust, especially in the thick and compositionally complex continental crust [45]. No significant fractions of HPEs are typically expected to be present in the Earth's metallic core due to their chemical affinity for silicates rather than metals.

Geoneutrinos are detected via the *Inverse Beta Decay* (IBD) reaction $\bar{\nu}_e + p \to e^+ + n$, a charged-current interaction that is sensitive exclusively to electron antineutrinos. Similar interactions are available to other antineutrino fla-

vors, but reactor and geoneutrinos do not have sufficient energy to produce μ^+ or τ^+ leptons. Organic liquid scintillators, such as the one used in JUNO, provide abundant free target protons for geoneutrino detection. The IBD interaction provides a powerful tool to suppress most backgrounds thanks to the strong space and time correlation between the prompt and delayed signals. However, reactor antineutrinos are detected by the very same process and thus represent an irreducible background in geoneutrino measurements.

The Borexino [40] and KamLAND [50] experiments observed geoneutrinos with high statistical significance, detecting 53 and 183 events respectively, and achieving relative precisions on the measured rate in the range of 15%–18%. The observed signals from both experiments—at widely separated locations, with Borexino in Italy and KamLAND in Japan—are consistent with geological predictions, but not precise enough to fully discriminate between different models. The SNO+ experiment in Canada reported the first detection of geoneutrinos in the Americas [60] and later improved this measurement, achieving a 26% precision on the geoneutrino rate [39].

The JUNO experiment [24, 9], located near the southern coast of China, will provide the first opportunity to detect geoneutrino signals on the continental margin. With its 20 kton target mass, JUNO will collect unprecedented geoneutrino statistics, surpassing within about a year the combined total sample detected by all other experiments to date. JUNO is located 52.5 km from two large nuclear power plants, making it an optimal facility for studying the neutrino mass ordering and making precision measurements of neutrino oscillation parameters [16, 8]. Despite the very significant irreducible background from reactor antineutrinos, JUNO is expected to achieve world-leading sensitivity to geoneutrinos shortly after the start of data taking.

JUNO's sensitivity to geoneutrinos was evaluated previously in Refs. [24, 48], but nearly nine years have passed since, during which significant progress has been made in detector design and in the understanding of the expected detector performance, reactor antineutrino flux, and backgrounds. This work presents a re-evaluation of JUNO's potential to measure the total geoneutrino signal, to disentangle the relative contributions from ^{232}Th and ^{238}U, and to recognize the mantle geoneutrino signal as an excess above the constrained lithospheric signal. Our sensitivity results span a broad range of signal strengths, enabling comparison with a wide variety of predictions from different geological models.

The paper is structured as follows. Section II presents an overview of the JUNO experiment and the detector design. Geoneutrinos are introduced in Section III, while Section IV elaborates on expected signal at JUNO site from lithosphere and mantle, building on various existing geological models. Signal event selection and expected backgrounds considered in the analysis are presented in Section V. The analysis procedure is explained in Section VI, the results of the sensitivity studies are shown in Section VII, and a brief conclusion is offered in Section VIII, and details of geoneutrino signal calculations at JUNO are provided in Appendix.

II. THE JUNO EXPERIMENT

The Jiangmen Underground Neutrino Observatory (JUNO) is a liquid scintillator detector [9] located at an approximate distance of 52.5 km from eight nuclear reactors in the Yangjiang and the Taishan nuclear power plants, in an underground laboratory with a vertical overburden of about 650 m (roughly 1800 m water equivalent) in the Guangdong Province in Southern China. The experiment's baseline is optimized for the primary goal of determining the neutrino mass ordering (NMO) through the interplay between the fast and slow oscillation patterns of reactor anti-neutrinos [16], a measurement that will also allow determining three oscillation parameters to sub-percent precision [8]. To achieve this, JUNO requires a large target mass and an excellent energy resolution, which offer further opportunities in neutrino and astroparticle physics [9, 2, 34, 11, 14, 6, 53, 10]. The JUNO collaboration will also deploy a satellite detector called the Taishan Antineutrino Observatory (TAO) that will provide a reference reactor antineutrino spectrum for JUNO's oscillation measurements [1].

A sketch of the JUNO detector is shown in Fig. 1. A Central Detector (CD) [13] contains the primary target consisting of 20 kton of a liquid scintillator mixture in a 17.7 m radius acrylic sphere. This makes JUNO the largest liquid scintillator detector ever built, in comparison with the 280 tons, 780 tons, and 1 kton active masses of Borexino [23], SNO+ [51], and KamLAND [36], respectively. The linear alkylbenzene (LAB)-based liquid scintillator mixture was optimized in dedicated studies using a Daya Bay detector [3]. The acrylic vessel (AV) is supported by a spherical stainless steel (SS) structure via 590 connecting bars. Scintillation light is detected by 17,612 20-inch photomultiplier tubes (PMTs) [7] and 25,600 3-inch PMTs facing the acrylic sphere that are mounted on the SS structure, providing a total photocathode coverage of 78%. These unique features lead to an energy resolution of $\approx 3\%/\sqrt{E(\mathrm{MeV})}$ [15], which is unprecedented for a detector of this type.

The CD is installed inside a cylindrical water pool (WP) 43.5 m in diameter and 44.0 m in height that is filled with 41 kton of ultra-pure water. The WP shields the CD against external radiation and acts as a Cherenkov veto detector for the residual cosmic-ray muon flux of 0.004 $\mathrm{m^{-2}s^{-1}}$. The veto system contains 35 kton of water, while an additional 6 kton of water are used in the CD

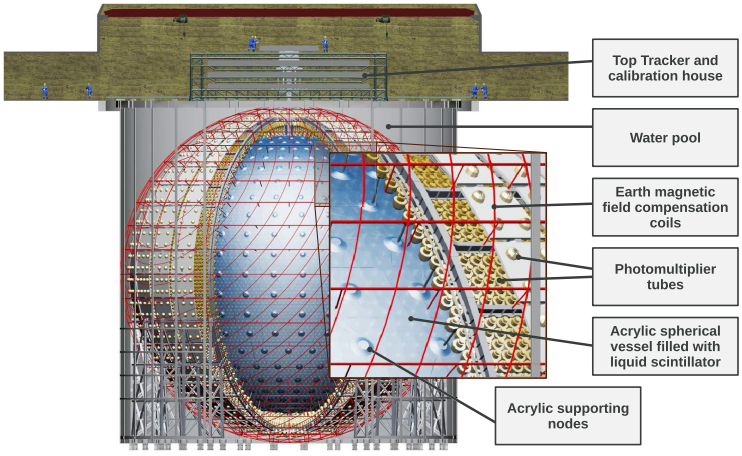


Fig. 1. (color online) Scheme of the JUNO Detector.

region between the SS and the AV. The WP veto is equipped with 2,400 20-inch PMTs installed on the outer surface of the SS structure. On top of the WP, a Top Tracker (TT) [12] is placed to precisely measure the tracks of a sub-sample of crossing muons.

A comprehensive multi-positional calibration system relying on various artificial and natural radioactive sources, as well as a pulsed laser, has been developed to calibrate the detector's spatial non-uniformity and energy scale non-linearity to sub-percent precision [5].

Detector construction was completed in late 2024, and liquid scintillator filling of the central target was completed on August 22, 2025.

III. GEONEUTRINOS

Geoneutrinos are emitted by HPEs that have persisted since the planet's formation from primordial material, primarily ^{232}Th ($T_{1/2}$ = 1.41(1) × 10^{10} years), ^{238}U ($T_{1/2}$ = 4.4683(96) × 10^{9} years), ^{235}U ($T_{1/2}$ = 7.0348(20) × 10^{8} years), and ^{40}K ($T_{1/2}$ = 1.262(2) · 10^{9} years) [45]. Natural thorium is fully composed of ^{232}Th, while natural uranium, largely dominated by ^{238}U, contains about 0.7204% of ^{235}U. Natural potassium contains only about 0.0117% of ^{40}K. Other HPEs exist, but their contributions are subdominant. In each decay, the emitted *radiogenic heat* is in a well-known ratio to the number of emitted geoneutrinos:

$$^{238}\mathrm{U} \rightarrow ^{206}\mathrm{Pb} + 8\alpha + 6e^- + 6\bar{\nu}_e, \mathrm{Q} = 51.7\ \mathrm{MeV} \quad (1)$$

$$^{235}\mathrm{U} \rightarrow ^{207}\mathrm{Pb} + 7\alpha + 4e^- + 4\bar{\nu}_e, \mathrm{Q} = 46.4\ \mathrm{MeV} \quad (2)$$

$$^{232}\mathrm{Th} \rightarrow ^{208}\mathrm{Pb} + 6\alpha + 4e^- + 4\bar{\nu}_e, \mathrm{Q} = 42.6\ \mathrm{MeV} \quad (3)$$

$$^{40}\mathrm{K} \rightarrow ^{40}\mathrm{Ca} + e^- + \bar{\nu}_e, \mathrm{Q} = 1.31\ \mathrm{MeV}\ (89.3\%) \quad (4)$$

$$^{40}\mathrm{K} + e^- \rightarrow ^{40}\mathrm{Ar} + \nu_e, \mathrm{Q} = 1.504\ \mathrm{MeV}\ (10.7\%) \quad (5)$$

The energies listed above represent total decay energies, of which geoneutrinos carry approximately 5% in the form of kinetic energy [28]. The corresponding energy spectra [21], shown in Fig. 2, all lie below 3.27 MeV. We note that the branch of the ^{238}U spectrum extending up to about 4.4 MeV is roughly three orders of magnitude lower and can therefore be considered negligible for the present study.

As mentioned in Section 1, the IBD reaction yields a positron and a neutron. The positron first deposits its kinetic energy before annihilating into two 511 keV γ-rays, generating a prompt signal with visible energy E_p that is directly correlated with the antineutrino energy $E_{\bar{\nu}_e}$:

$$E_p \sim E_{\bar{\nu}_e} - 0.78\ \mathrm{MeV}. \quad (6)$$

The capture of the thermalized neutron occurs primar-

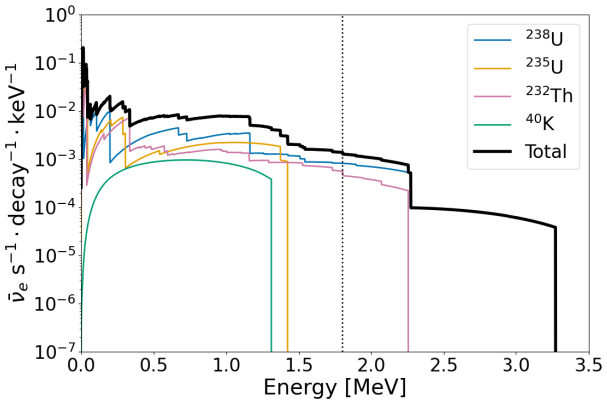


Fig. 2. (color online) Geoneutrino energy spectra [21] from the decays of the ^{238}U, ^{235}U, and ^{232}Th chains and of ^{40}K. The total spectrum integrals are 6 for ^{238}U, 4 for ^{235}U and ^{232}Th, and 0.89 for ^{40}K. The vertical dotted line indicates the kinematic threshold of the IBD interaction.

ily on a free proton or with ∼1% probability on ^{12}C. It is followed by a γ-ray emission (2.22 MeV or 4.9 MeV for capture on H or ^{12}C, respectively) that constitutes the delayed signal. The tight temporal and spatial coincidence between the prompt and delayed signals provides a clear signature for $\bar{\nu}_e$ events that allows to effectively suppress backgrounds.

The IBD cross-section is precisely known, with an uncertainty of about 0.4% [56]. The reaction is sensitive only to the electron neutrino flavor and has a kinematic threshold of 1.806 MeV. As shown in Fig. 2, ^{40}K and ^{235}U geoneutrinos fall below the IBD threshold. Only 0.38 and 0.15 antineutrinos per decay of ^{238}U and ^{232}Th, respectively, exceed this threshold, with maximal energies of 3.27 MeV and 2.25 MeV.

The geoneutrino signal is often expressed in *Terrestrial Neutrino Units* (TNU), which simplifies the conversion between geoneutrino flux and IBD event rates. One TNU corresponds to one IBD event per year in a detector with 100% efficiency and 10^{32} free target protons (approximately 1 kton of LS).

Estimating the abundance of a given HPE in the bulk Earth relies on modeling. *Bulk Silicate Earth* (BSE) models integrate cosmochemical, geochemical, and geophysical data to estimate the composition of the primordial bulk silicate Earth, after the separation of the metallic core. While there are several categories of BSE models (see also Section IV.B), they typically predict a few 10^{16} kg of uranium, 10^{17} kg of thorium, and 10^{20-21} kg of potassium [40].

Considering the natural abundances of radioactive isotopes and their specific radiogenic heat, the Earth's total radiogenic heat is predicted to range from about 10 to 37 TW [30]. All BSE models predict an almost equal contribution from U and Th to the radiogenic heat, while ^{40}K is expected to contribute about 14%–17% due to its lower elemental specific heat production. The corresponding average surface geoneutrino flux is on the order of 10^7 cm^{-2} s^{-1}, which yields a geoneutrino signal S ranging from a few to several tens of TNU, depending on the location.

Measurement of the geoneutrino signal can provide important information about the Earth's radiogenic heat, HPE distribution and, consequently, the processes involved in Earth's formation. While different BSE models predict HPE abundances that vary by a factor of 2 to 3, all models predict similar proportions of HPEs. This consistency is based on the observed strong correlation of isotopic ratios in the solar photosphere and meteorites [29]. This is particularly important given that present-day detection techniques are not yet capable of measuring ^{40}K geoneutrinos. An experimental confirmation of the Th/U ratio consistent with theoretical expectations would validate existing models and increase confidence in extrapolating the Earth's total radiogenic heat from U, Th, and K based solely on measurements of U and Th geoneutrinos.

The primordial BSE later differentiated into the present-day crust and mantle. This process redistributed HPEs, which are characterized by high concentrations in the crust. For a more precise estimation of the geoneutrino signal expected at a specific location, several geological factors, as well as the local geology around the experimental site, must be considered. This is broadly discussed in the next section for the case of JUNO in South China.

IV. EXPECTED GEONEUTRINO SIGNAL AT JUNO

The evaluation of the expected geoneutrino signal requires knowledge of the abundances and distribution of HPEs inside the Earth as the key inputs. Due to their geochemical affinity, HPEs concentrated in the silicate part of the Earth after the formation of the metallic core [44, 65]. During the differentiation of the silicate Earth, HPEs were concentrated in the continental crust, as their ionic properties favor partitioning into silicate melts and upward transport by magmatism. While the composition of the more accessible, shallow layers of the Earth can be constrained through rock sample analysis and high-resolution geophysical data, the abundances of elements in the mantle are inferred indirectly from geochemical arguments and BSE compositional models.

For detectors situated on the continental crust, such as JUNO, the geoneutrino signal is predominantly influenced by the area within a few hundred kilometers around the experimental site [68]. In this work we present JUNO's sensitivity to geoneutrinos in a model independent way. In order to anchor the range of considered expected signals, we provide an overview of different models that predict the signal from the lithosphere (Section IV.A) and mantle (Section IV.B), with further details provided in the Appendix. Figure 3 presents a schematic of the Earth's structure highlighting the components important for the geoneutrino signal calculation.

The oscillation of geoneutrinos during their propagation from their production site to JUNO must, in principle, be considered. However, even though studies performed between 2015 and 2020 used different oscillation parameter sets available at the time, their impact is small compared to the much larger uncertainties in geological models and input assumptions.

A. Lithospheric contribution

The lithosphere consists of the Earth's crust and the underlying Continental Lithospheric Mantle (CLM), which is mechanically coupled to the crust but significantly poorer in HPEs. For detectors situated on the continental crust, such as JUNO, the geoneutrino signal is predominantly (40%−80%) influenced by the adiajcent

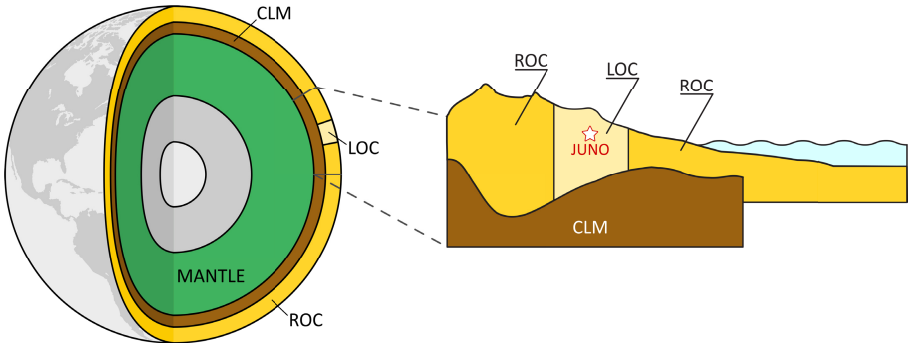


Fig. 3. (color online) Schematic drawing (not to scale) of the Earth's structure highlighting the components contributing to the geoneutrino signal expected at JUNO: the mantle, the Continental Lithospheric Mantle (CLM) and the crust. The crust is divided into the Local Crust (LOC), defined as the portion within a few hundred kilometers from the detector, and the Rest of the Crust (ROC).

lithosphere, primarily from the Local Crust (LOC), the region within a few hundred kilometers of the detector. Detailed geological information from the LOC has a larger impact on the prediction with respect to the Rest Of the Crust (ROC) and CLM.

For this study, the geoneutrino signals from the LOC, ROC, and CLM reported in previous works were analyzed (Fig. 3). All models employ different methodologies and approaches with variations in the size and coordinates of the LOC but remain strongly correlated due to partially shared geophysical and geochemical inputs. In particular, we considered the following models:

1. The global Refined Reference Earth Model (RRM) [68] for HPEs' abundances and distribution is exploited for the prediction at JUNO site in Ref. [61].

2. GIGJ (GOCE Inversion for Geoneutrinos at JUNO) [43] is a 3D model exploiting local gravimetric data (GOCE), seismic data, and HPE abundances from RRM.

3. Wipperfurth *et al.* (W20) [63] considers three different geophysical models CRUST2.0 [18] (W20 [C2.0]), CRUST1.0 [31] (W20 [C1.0]), and LITHO1.0 [41] (W20 [L1.0]), while the HPE abundances are derived using a strategy similar to the RRM.

4. JULOC [47] incorporates a 3D model of the LOC using as geophysical input a 3D shear wave velocity model inverted from seismic ambient noise tomography. The geochemical inputs are based on U and Th abundances from over 3000 rock samples in the region and from global U and Th databases.

Figure 4 compares the prediction of all six models. Most models report a lithospheric geoneutrino signal $S_{\rm LS}(\rm U+Th)$ with a central value in the range of 28.9 TNU to 32.0 TNU, with an average relative uncertainty of about 20% (Appendix, Table A2). Instead, JULOC stands out with a much larger signal of $S_{\rm LS}(\rm U+Th) = 40.4$TNU

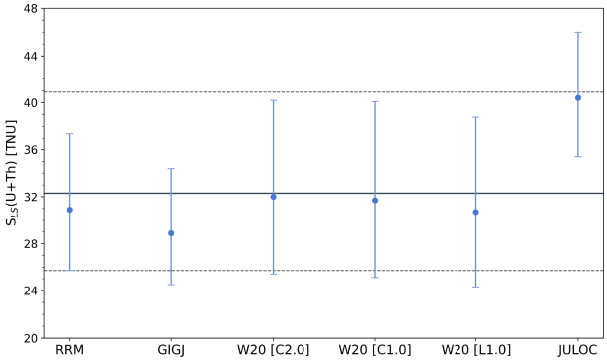


Fig. 4. (color online) Predicted geoneutrino signals S(U+Th) for the six lithospheric models, with error bars representing the corresponding 1σ uncertainties. The solid horizontal line marks the central value of the combined signal, while the dashed lines indicate its 1σ bounds.

and a lower relative uncertainty of about 10%. The ratios of S(Th)/S(U) remain consistent across all models, with values clustering around 0.30–0.31. This stability reflects the strong correlation between U and Th contributions and highlights the uniformity in the assumed Th/U abundance ratio across the models.

Since all these models share some common features, it is necessary to account for strong correlations when calculating a single central value and the corresponding uncertainty for the expected lithospheric signal at JUNO. A combined prediction has been derived by a study in which 10^6 values of geoneutrino signals were generated for each model. The resulting combined prediction for the lithospheric geoneutrino signal at JUNO was $S_{\rm LS}(\rm U) = 24.7^{+6.7}_{-5.5}$ TNU and $S_{\rm LS}(\rm Th) = 7.5^{+2.2}_{-1.8}$ TNU. The combined prediction was $S_{\rm LS}(\rm U + Th) = 32.3^{+8.6}_{-6.6}$ TNU, with a signal ratio $S_{\rm LS}(\rm Th)/S_{\rm LS}(\rm U)$ of 0.30 (Appendix, Table A2).

B. Mantle contribution

Since direct access to the deep mantle is impossible, the BSE models integrate cosmochemical, geochemical, and geophysical data to estimate the HPE distribution.

Cosmochemical constraints are grounded on chondritic meteorites, particularly carbonaceous [46] and enstatite chondrites [42], considered proxies for the building blocks of Earth. Also, geochemical data from Mid-Ocean Ridge Basalts provide direct insights into the upper mantle's composition [37]. Geophysical evidence from seismic wave velocities, surface heat flow and mantle density profiles further constrain mantle composition [59].

A broad range of BSE compositional models has been proposed, which can be categorized based on their predicted radiogenic heat production (H) into three classes: (1) poor-H models, (2) medium-H models, and (3) rich-H models. Poor-H models, based on enstatite chondrites, predict low U and Th abundances, resulting in a total radiogenic heat $H_{\rm BSE}^{\rm Poor} = 12.4 \pm 1.9$ TW. Medium-H models assume relative refractory lithophile element abundances similar to CI chondrites, calibrated with terrestrial samples, and predict $H_{\rm BSE}^{\rm Medium} = 19.7 \pm 3.1$ TW. Rich-H models, which include geodynamic models based on mantle convection energetics, predict higher radiogenic heat outputs at $H_{\rm BSE}^{\rm Rich} = 31.7 \pm 3.4$ TW (Table 17 of Ref. [30]).

Once the total U and Th content is fixed for a given BSE class, and the lithospheric U and Th abundances are determined ($H_{\rm LS} = 6.9^{+1.6}_{-1.2}$ TW), [68]), the residual amounts of U and Th in the mantle are calculated by subtracting the lithospheric contribution from the total BSE estimates (Table 29 of Ref. [30]). The mantle radiogenic heat obtained for each BSE class (Table 1) reflects the assumptions regarding the Earth's primordial composition and an assumed model for the LS. The expected mantle geoneutrino signal is obtained by applying a linear relationship between the radiogenic heat generated by U and Th in the mantle and the corresponding signal. The proportionality coefficient accounts for the spatial distribution of HPEs and is independent of their absolute abundance. For each BSE class, the uncertainty on the signal S_M(U + Th), as reported in Table 1, reflects both the compositional variability within each model and the uncertainty related to the distribution of HPEs in the mantle. The methodology outlined in the Appendix enables a consistent estimation of the expected signal ranges for the various BSE models. As a consequence, the relative uncertainties vary significantly: the Poor-H model exhibits the highest average relative uncertainty (~80%), whereas the Rich-H model shows the lowest (~30%) (Table 1).

Table 1. Mantle radiogenic heat production from U, Th and K ($H_{\rm M}$(U + Th + K)) and from U and Th alone ($H_{\rm M}$(U + Th)) for the three classes of Bulk Silicate Earth (BSE) model: Poor-H, Medium-H and Rich-H. The mantle geoneutrino signal ($S_{\rm M}$(U + Th)) is derived using the linear relationship discussed in Appendix. The U and Th components are calculated based on the relation between the signal ratio ($S_{\rm M}$(Th)/$S_{\rm M}$(U)) and the mass ratio of Th to U ($M_{\rm Th}/M_{\rm U}$), the latter predicted by BSE.

	Poor-H	Medium-H	Rich-H
Mantle radiogenic heat [TW]			
H_M(U+Th+K)	$4.2^{+2.4}_{-2.6}$	$11.4^{+3.5}_{-3.6}$	$23.4^{+3.8}_{-3.9}$
H_M(U+Th)	$3.2^{+2.0}_{-2.1}$	$9.3^{+2.9}_{-2.9}$	$20.2^{+3.2}_{-3.3}$
Mantle geoneutrino signal [TNU]			
S_M(U)	$2.4^{+2.1}_{-1.7}$	$6.5^{+3.2}_{-2.6}$	$13.7^{+4.5}_{-3.7}$
S_M(Th)	$0.4^{+0.3}_{-0.3}$	$1.5^{+0.7}_{-0.6}$	$3.6^{+1.2}_{-1.0}$
S_M(U+Th)	$2.8^{+2.4}_{-1.9}$	$8.0^{+4.0}_{-3.2}$	$17.4^{+5.7}_{-4.7}$
Mantle geoneutrino signal ratio			
S(Th)/S(U)	0.17	0.23	0.26

Given its proportionality to the mass ratio $M_{\rm Th}/M_{\rm U}$, the signal ratio $S_{\rm M}$(Th)/$S_{\rm M}$(U) varies across the compositional models, with the Poor-H class reporting the lowest ratio (0.17), corresponding to a higher relative U abundance (see Section 2.1 in [28]). In contrast, the relatively higher Th abundance in the Rich-H class leads to the highest value of $S_{\rm M}$(Th)/$S_{\rm M}$(U) = 0.26. We note that this variability is primarily a consequence of different mobility of uranium and thorium and different enrichment in the crust over geological time, while the bulk $M_{\rm Th}/M_{\rm U}$ in all BSE models is close to a chondritic value of about 3.9 [30, 40, 64].

It is worth mentioning that the uncertainty of the lithospheric signal $\left(S_{\rm LS} = 32.3^{+8.6}_{-6.6}\text{TNU}\right)$ is larger than the central value of the Poor-H mantle signal $\left(S_{\rm M} = 2.8^{+2.4}_{-1.9}\text{TNU}\right)$ and comparable to that of the Medium-H mantle signal $\left(S_{\rm M} = 8.0^{+4.0}_{-3.2}\text{TNU}\right)$. This highlights the critical need for refining the local crustal model and reducing the lithospheric uncertainty to enable identification of the mantle signal above the constrained lithospheric contribution, as discussed in Sec. VII.C.

C. Total signal

The total geoneutrino signal at JUNO is determined by combining the lithospheric contribution $S_{\rm LS} = 32.3^{+8.6}_{-6.6}$ TNU, calculated based on estimates from published models, with the mantle signal, evaluated according to the three compositional classes of BSE (Table 1). This approach results in three distinct total geoneutrino signals: one representing to the Poor-H model, one for the Medium-H model, and one for the Rich-H model (Table 2). The corresponding total geoneutrino signal, including uncertainties, spans the range from 28.6 TNU to 60.3 TNU. This interval is fully covered in our scan of JUNO's sensitivity to different geoneutrino signal strengths ranging from 20 to 70 TNU, as presented in Sections VII.A and VII.B.

The uncertainties on the total geoneutrino signals for the Poor-H, Medium-H, and Rich-H models from Table 2

Table 2. Total geoneutrino signals obtained summing the combined lithospheric signal and the mantle signals for the three BSE models (Poor-H, Medium-H, Rich-H). The uncertainties include contributions from the lithosphere and the mantle, treated as independent. The U and Th components are reported together with their ratio.

	S(U) [TNU]	S(Th) [TNU]	S(U+ Th) [TNU]	S(Th)/S(U)
Poor-H	$28.1^{+8.2}_{-6.2}$	$8.1^{+2.3}_{-1.8}$	$36.0^{+9.6}_{-7.4}$	0.29
Medium-H	$32.0^{+7.9}_{-6.4}$	$9.1^{+2.4}_{-1.9}$	$41.0^{+9.5}_{-7.7}$	0.29
Rich-H	$39.1^{+8.3}_{-6.9}$	$11.3^{+2.5}_{-2.1}$	$50.2^{+10.1}_{-8.5}$	0.29

were calculated by treating the contributions from the lithosphere and the mantle as linearly independent, taking into account that the errors associated with the lithospheric signal and those linked to the mantle signal are uncorrelated. The asymmetrical uncertainties, reflecting the non-Gaussian nature of the distributions, are propagated using the probability density functions of each component. We note that for each model, the total uncertainty is dominated by the uncertainty associated with the lithospheric contribution, which reflects variability in the crustal model and published estimates. The roughly ± 7 TNU spread of the central values among the three models represents the variability of the mantle signal prediction.

The individual contributions of U and Th to the total geoneutrino signal have been computed, allowing the calculation of the S(Th)/S(U) ratios. Independently of the considered BSE class, the ratio of the total signal remains constant at 0.29 (Table 2), as it is predominantly controlled by the lithospheric contribution, which strongly influences the thorium-to-uranium signal balance.

V. EVENT SELECTION AND EXPECTED BACKGROUNDS

The space and time coincidence signature of the IBD interaction, used to detect geoneutrinos, provides excellent means of background suppression. The selection criteria for IBD candidates are described in Section V.A. Reactor antineutrinos, detected through the same IBD process, constitute an irreducible background in geoneutrino detection, as will be detailed in Section V.B. Other non-antineutrino backgrounds must be thoroughly evaluated too, as discussed in Section V.C.

A. IBD event selection

Geoneutrinos are detected via the same IBD reaction as reactor antineutrinos and the analysis of both is performed on the prompt energy spectrum from the IBD threshold up to the end point of reactor spectrum (see Section VI). Consequently, the selection of IBD event candidates is the same for geoneutrino analysis, as in the previous JUNO sensitivity studies regarding reactor antineutrinos [16, 8]. A fiducial volume (FV) cut of 17.2 m away from the detector center (within a distance of 0.5 m from the inner surface of the AV) is applied in order to reduce the external background. The prompt IBD candidate events are restricted to the energy window [0.8, 12.0] MeV. The delayed candidate must have energies in the windows of [1.9, 2.5] MeV or [4.4, 5.5] MeV, corresponding to the capture on Hydrogen and Carbon, respectively. Then, a correlation between a prompt and delayed candidate is searched by requiring a separation of no more than 1.0 ms in time and 1.5 m in space. This will greatly reduce the contribution of uncorrelated events. Lastly, a complex veto for cosmic muons and cosmogenic events, in particular neutrons and ^{9}Li/^{8}He, is applied. When all cuts are applied in sequence, the overall tagging efficiency for IBD events is 82.2% including the effect of FV (91.5%) and muon veto (91.6%).

B. Reactor antineutrino background

1. *Nearby reactors within 300 km*

Reactor antineutrinos from the nearby power plants constitute the largest background for the geoneutrino measurement, with a dominant contribution from the Taishan and Yangjiang power plants. This background also includes antineutrinos from Daya Bay power plant at a distance of 215 km. For each core, the antineutrino flux expected at JUNO from the fission of ^{235}U, ^{238}U, ^{239}Pu, and ^{241}Pu is estimated from the Huber-Mueller model [32, 57], weighed with the IBD cross section [56], and corrected with the Daya-Bay observation [27]. Fission fractions of 0.58, 0.07, 0.30, and 0.05 for ^{235}U, ^{238}U, ^{239}Pu, and ^{241}Pu, respectively, as well as the Q values of the decays of these isotopes, are taken from Ref. [66]. Corrections accounting for non-equilibrium and spent nuclear fuel contributions are applied to the spectra. This procedure, which is the same used in Refs. [16, 8], yields a reactor antineutrino rate of 43.2 events per day (1336.2 TNU), assuming an IBD selection with 82.2% efficiency and an average reactor duty cycle of 11/12 to account for refueling outages. The energy spectrum of reactor antineutrinos extends well beyond the geoneutrino end point, reaching up to about 12 MeV. For geoneutrino studies, a prompt energy window up to 2.6 MeV is typically used to fully capture the signal while accounting for detector resolution. Within this window, the corresponding background is 10.7 events per day (332.5 TNU). The spectral differences between reactor and geoneutrinos, as well as the information in the spectrum above the geoneutrino end point, provide strong leverage to constrain the react-

or contribution and isolate the geoneutrino signal with high precision. In this work, we use the existing constraints on the unoscillated reactor antineutrino spectral shape from the Daya Bay experiment [26], supplemented by an additional uncertainty to account for potential fine-structure effects not resolved by Daya Bay due to its lower energy resolution. This uncertainty, which amounts to about 2% for most of the energy region, is estimated from a comparison between the Daya Bay measurement and a summation model [22]. We do not apply the TAO-based constraints used in Refs. [16, 8], since a geoneutrino measurement can be achieved with significantly lower statistics than required for the neutrino mass ordering measurement, at which point TAO results may not yet be fully available. Moreover, while TAO constraints are important for JUNO's measurement of the mass ordering and the Δm^2_{31} oscillation parameter, we find that geoneutrino sensitivities are only marginally improved by their inclusion, even at higher exposures, owing to the smooth and relatively broad nature of the geoneutrino spectrum.

2. *World reactors beyond 300 km*

World reactors refer to reactor antineutrinos originating from commercial reactors located more than 300 km from the JUNO site. In this analysis, their contribution has been updated using the latest available data from the International Atomic Energy Agency (IAEA). The Power Reactor Information System (PRIS) [33] provides annually data on reactors worldwide, including their nominal thermal power and monthly load factors. Using this information, energy spectra per fission of ^{235}U, ^{239}Pu, and ^{241}Pu is obtained, using for each reactor the same flux parametrization and core composition as for the nearby reactors described above.

We observe a steady increase of the world reactor background. Since 2019 used in [16, 8], in 2024 the calculated rate is about 30% higher, mainly due to new reactors in China. Consequently, the world reactor rate has been updated to the latest calculation of 42.2 TNU, corresponding to 1.4 IBD events per day after IBD selection in JUNO. To account for the unknown yearly increase, the rate uncertainty has been increased to 10%. Although the shape of the yearly spectra changes, it was found that updating it has no impact on the geoneutrino measurement, when in the analysis its rate is constrained to the expected value. Therefore, we use the same 5% shape uncertainty as in [16, 8].

C. Other backgrounds

For this analysis, the non-reactor backgrounds — excluding the updated ^{13}C(α, n)^{16}O background — are the same as those used in the neutrino mass ordering [16] and neutrino oscillation parameters [8] sensitivity studies. All backgrounds are summarized in Table 3.

Table 3. Expected event rates after IBD selection including muon veto and FV cut (Section V.A) for geoneutrinos and the different backgrounds. For the former, the quoted interval represents the 1σ band covering all models from Table 2, e.g. 28.6 to 60.3 TNU. Individual ^{238}U and ^{232}Th contributions are calculated assuming the chondritic mass ratio. For backgrounds, we indicate the total rate as well as the rate within the geoneutrino window with prompt energy E_p below 2.6 MeV. The last two columns show the rate and shape uncertainties, respectively, applied in this analysis.

Component	Rate		Rate Unc.	Shape Unc.
	R	R^{geo}	σ^{rate}	σ^{shape}
	Total	$E_p < 2.6$ MeV		
	[day^{-1}]	[day^{-1}]	[%]	[%]
Geoneutrinos (^{238}U + ^{232}Th)	0.92–1.95	0.92–1.95	-	5
Geoneutrinos (^{238}U)	0.71–1.50	0.71–1.50	-	5
Geoneutrinos (^{232}Th)	0.21–0.45	0.21–0.45	-	5
Reactor antineutrinos	43.2	10.7	-	Daya Bay [26]
World reactors	1.4	0.4	10	5
Accidentals	0.8	0.7	1	0
^{9}Li/^{8}He	0.8	0.1	20	10
Atmospheric neutrinos	0.16	0.03	50	50
Fast neutrons	0.1	0.02	100	20
^{13}C(α, n)^{16}O	0.090	0.063	25	25

After reactor antineutrinos, the most significant background is the accidental background, formed by the coincidence of two uncorrelated events. Its expected rate of 0.8 events per day is estimated from radioactivity measurements of the various components of the JUNO detector [4]. A 1% uncertainty is assigned to the overall rate, while the shape uncertainty is very small due to the precise determination of the energy spectrum using an off-window method, whereby an artificial delayed window, shifted by an arbitrarily long time after the prompt candidate, is used to form uncorrelated pairs.

An effective muon veto system is expected to suppress the cosmogenic ^{9}Li/^{8}He background to the same level as the accidental background, approximately 0.8 events per day. This background can also be reliably estimated using independent data samples in real data. In particular, the identification of IBD-like coincidences that are spatially and temporally correlated with cosmic muons enables the evaluation of untagged β-neutron decays from ^{9}Li/^{8}He.

IBD-like background events from atmospheric neutrinos, fast cosmogenic neutrons, and the $^{13}C(\alpha, n)^{16}O$ reaction are expected to occur at significantly lower rates. These contributions carry larger uncertainties, as they typically cannot be fully constrained by data and must instead be estimated through Monte Carlo simulations informed by experimental inputs.

The $^{13}C(\alpha, n)^{16}O$ background has been recently revised [58] using state-of-the-art simulations of the interaction. Alpha particles emitted by intrinsic contaminants such as ^{238}U, ^{232}Th, and $^{210}Pb/^{210}Po$ can be captured on ^{13}C nuclei, resulting in the emission of MeV-scale neutrons. A prompt signal can arise before the delayed neutron capture from neutron elastic scattering on protons, de-excitation γ rays emitted by ^{16}O nuclei produced in excited states, or inelastic interactions of the outgoing neutron with ^{12}C, yielding a signature that mimics that of an IBD signal. The open-source SaG4n software [20] was used to calculate the energy depositions from the neutron and any associated ^{16}O de-excitation products. The detector response was simulated with JUNO's Geant4-based full simulation framework. After application of the IBD selection criteria described in Section V.A, the expected rate is 0.090 events per day, with 25% uncertainties in both rate and shape. This update nearly doubles the previous expectation reported in JUNO studies [16, 8], as it now accounts for unsupported ^{210}Po, and simultaneously reduces the associated uncertainties by about a factor of two. Given the expected levels of α contamination in the LS and the constraints applied to this background during the fit, this update has a minimal impact on the geoneutrino measurement in the present study. In the future, the α contamination will be assessed directly from data, providing a means to constrain this background.

VI. ANALYSIS STRATEGY

This section presents the analysis strategy employed to study JUNO's sensitivity to geoneutrinos. Section VI.A outlines the construction of input spectral shapes and the incorporation of the detector response. The fitting procedure, based on a binned χ^2 method utilizing either a covariance matrix or pull terms, is described in Section VI.B, along with the treatment of systematic uncertainties. To assess the sensitivities and validate the robustness of the results, both Asimov and toy pseudo-experiment datasets are used, as detailed in Section VI.C. The strategy to assess JUNO's discovery potential for the mantle geoneutrino signal is presented in Section VI.D.

A. Input spectral shapes

The prediction of the reconstructed prompt energy spectra of the geoneutrino IBD signal and the reactor antineutrino background is carried out using two complementary approaches. The first relies on analytical parameterizations of the IBD reaction kinematics, the liquid scintillator non-linearity, and JUNO's energy resolution [15], while the second employs large-scale datasets produced with JUNO's full simulation framework. The former approach is the same as used in previous sensitivity studies [16, 8], and it reproduces the same spectra. For geoneutrinos, the contributions from ^{238}U and ^{232}Th were simulated separately, and both were found to be in excellent agreement with the analytical spectra. It is worth noting that our analysis accounts for possible spectral distortions in the geoneutrino spectrum arising from neutrino oscillations and the heterogeneous distribution of HPEs by assuming a 5% shape uncertainty, which encompasses these effects. For the extraction of the TNU geoneutrino signal in real data analysis, only the spectral deformation is relevant. The effect of oscillation on the expected event rate is, however, included in the TNU signal prediction of different models, as described in more detail in Appendix. An average constant survival probability of 55% is assumed for the mantle, while for the lithosphere we use directly the TNU values predicted by the authors of each model. Reactor neutrinos were simulated unoscillated, as the oscillated spectra can be obtained by applying the survival probability. Small differences with respect to the analytical spectra were observed but found to have a negligible impact on the resulting sensitivities. The remaining background spectra are modeled with the analytical approach. The accidental spectrum is derived from the latest characterization of detector materials, incorporating the energy, position, and rate of uncorrelated radioactive events [4]. The spectrum of cosmogenic ^{9}Li–^{8}He is adopted from the calculation benchmarked at Daya Bay [25], and the fast neutron contribution is taken to be flat. The "world reactors" spectrum, arising from cores located more than 300 km from JUNO, has been discussed in Section V. Except for the (α,n) background, whose rate and spectral shape have been updated with a dedicated Monte Carlo simulation (see Section V.C), all of these spectra are unchanged from previous analyses.

The resulting spectral shapes of geoneutrinos, reactor neutrinos, and other backgrounds, normalized to their expected rates under 1 year of exposure as given in Table 3 and for a 40 TNU geoneutrino signal, are shown in Fig. 5. We adopt the values of the oscillation parameters from PDG 2024 [52] as nominal.

B. Fitting procedure

We perform our sensitivity studies using the binned χ^2 method. We fit the energy spectrum of the prompt IBD candidates from 0.8 MeV to 12.0 MeV, and adopt a differential binning strategy to avoid bins with zero or very low bin content in realistic datasets. Specifically, the region between 1 and 7 MeV is divided into 20 keV bins, while the lower and higher energy regions have bin widths that range between 0.2 and 2 MeV, such that the

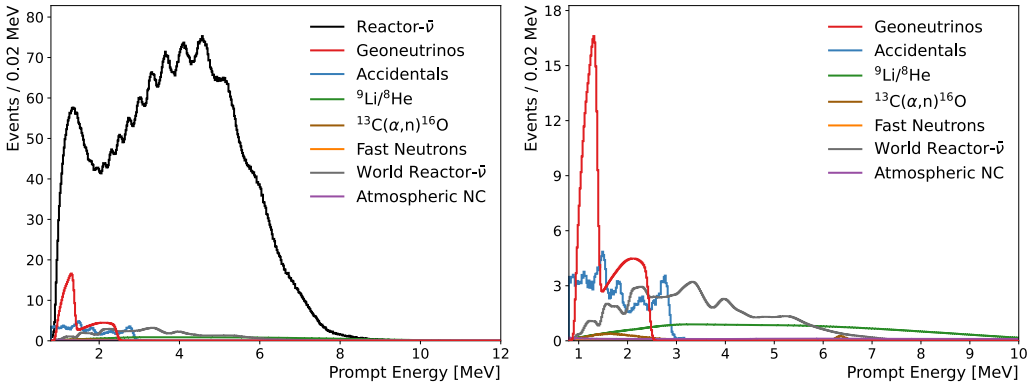


Fig. 5. (color online) (a) Spectral shapes of geoneutrinos, reactor neutrinos, and other backgrounds normalized to 1 year of exposure using the expected rates from Table 3, with 40 TNU for geoneutrino signal. Total geoneutrino spectrum shown in red corresponds to ^{238}U and ^{232}Th components fixed according to chondritic ratio. (b) A zoomed-in version of (a) with reactor spectrum removed in order to better appreciate comparison of geoneutrino spectra with different backgrounds.

probability of having a fluctuation to zero with one year of exposure is less than 0.02%. The fits are performed using a total of 314 energy bins and with the iMINUIT package in Python [19, 35].

The combined Neyman-Pearson (CNP) χ^2 is used for minimization as it is found to have the least bias with low statistics compared to other test statistics [67]. The basic CNP χ^2 that only includes statistical uncertainty can be written as:

$$\chi^2_{\rm CNP} = \sum_{i=1}^{\rm Nbins} \frac{(T_i(\boldsymbol{\theta}) - M_i)^2}{3\Big/\left(\frac{1}{M_i} + \frac{2}{T_i(\boldsymbol{\theta})}\right)}. \tag{7}$$

Here, M_i represents the measured number of events. The template model number of events, $T_i(\boldsymbol{\theta})$, depends on the vector of fit parameters $\boldsymbol{\theta}$ and is the sum of geoneutrinos, reactor antineutrinos, and other background events, in the i-th energy bin. Fit parameters include the oscillation parameters $\sin^2\theta_{12}$, Δm^2_{21}, Δm^2_{31}, and $\sin^2\theta_{13}$, the number of reactor antineutrinos $N_{\rm rea}$, and the number of geoneutrinos $N_{\rm geo}$. The latter parameter is used when Th/U ratio is fixed in the fit, while parameters $N_{\rm U}$ and $N_{\rm Th}$ are used instead of $N_{\rm geo}$ when the ^{238}U and ^{232}Th components are fit independently. All the oscillation parameters are left free in the fit without constraints. Applying the Daya Bay constraint on $\sin^2\theta_{13}$ [17], which is more precise than any JUNO measurement, has very little impact on the sensitivities.

The systematic uncertainties considered in the fit include the rate ($\sigma^{\rm rate}$) and spectral shape ($\sigma^{\rm shape}$) of the different components, as listed in Table 3. The non-linearity of the liquid scintillator energy scale for positrons is also considered following the same approach described in Refs. [16, 8], under the assumption that a calibration precision comparable to that achieved at Daya Bay can be obtained. In this approach, four representative curves corresponding to typical one-sigma variations are randomly weighted to span the full uncertainty range. Other effects such as the uncertainties on the non-equilibrium and spent nuclear fuel corrections applied on the reactor spectrum, the error on JUNO's energy resolution, and the uncertainty on the Earth's matter density used in the neutrino oscillation formula, were found to have a negligible impact and are thus not considered.

The uncertainties are treated through both covariance matrices and pull terms. In general, the two approaches yield consistent results, and any small residual differences are included in the systematic uncertainty of the final result. In the covariance matrix approach, the CNP χ^2 with all sources of uncertainty becomes:

$$\chi^2_{\rm CNP-CM} = \sum_{i,j=1}^{N_{\rm bins}} (M_i - T_i(\boldsymbol{\theta})) \cdot V^{-1}_{ij} \cdot (M_j - T_j(\boldsymbol{\theta})), \tag{8}$$

where i and j are represent the energy bins in a two-dimensional covariance matrix V_{ij}. We note that, in the statistics-only case, $V_{ij} = V^{\rm stat}_{ij}$ is diagonal and becomes identical to the denominator in Eq. (7),

$$V^{\rm stat}_{ij} = 3\Big/\left(\frac{1}{M_i} + \frac{2}{T_i(\boldsymbol{\theta})}\right), \tag{9}$$

thus showing the equivalence between the two approaches. When systematic uncertainties are included, the systematic covariance matrix $V^{\rm syst}_{ij}$ is constructed by summing the individual systematic uncertainty matrices that include the rate and shape uncertainties of the spectral components and the non-linearity effect, and the total covariance is given by $V_{ij} = V^{\rm stat}_{ij} + V^{\rm syst}_{ij}$. The shape uFncer-

tainties of all the spectral components $\sigma^{\rm shape}_{\rm sp,i}$ are modeled as bin-to-bin uncorrelated and the rate uncertainties of the backgrounds $\sigma^{\rm rate}_{\rm b}$ as bin-to-bin correlated. The uncertainties for each spectral component were estimated individually using the methods explained in Section V. The non-linearity uncertainty is propagated through the detector response model parameters, and the corresponding covariance matrix is obtained by generating 10,000 ($N_{\rm exps}$) fluctuated spectra with the fluctuated non-linearity curves and computing the difference between the nominal spectrum and the fluctuated spectra. The complete systematic covariance matrix can thus be written as

$$V^{\rm syst}_{ij} = \sum_{sp=1}^{N_{\rm spectra}} (\sigma^{\rm shape}_{{\rm sp},i})^2 M_i \cdot M_i + \sum_{b=1}^{N_{\rm bckgs}} (\sigma^{\rm rate}_{{\rm b},i})^2 M_i \cdot M_j + \frac{1}{N_{\rm exps}} \sum_{k=1}^{N_{\rm exps}} (M_i - x^k_i)(M_j - x^k_j), \tag{10}$$

where x^k represents the bin content of the k-th fluctuated spectrum.

In the pull-term approach, the χ^2 is written as:

$$\chi^2_{\rm CNP-pull} = \sum_{i=1}^{N_{\rm bins}} \frac{(T_i(\boldsymbol{\theta}) - M_i)^2}{3 \Big/ \left(\frac{1}{M_i} + \frac{2}{T_i(\boldsymbol{\theta}) + \left(\sum_{sp=1}^{N_{\rm spectra}} T_i(\boldsymbol{\theta}) \cdot \sigma^{\rm shape}_{sp,i} \right)^2} \right)} + \sum_{b=1}^{N_{\rm bckgs}} \left(\frac{T_b(\boldsymbol{\theta}) - \bar{\eta}_b}{\sigma^{\rm rate}_b} \right)^2 + \sum_{l=1}^{4} \alpha^2_l. \tag{11}$$

Here, the shape uncertainties $\sigma^{\rm shape}$ (Table 3) of all components are added in quadrature with the statistical uncertainties in each bin. The fitted number of events for each background b, $T^b(\boldsymbol{\theta})$, is constrained with a penalty term, where $\bar{\eta}_b$ denotes the expected number of events and $\sigma^{\rm rate}_b$ the associated rate uncertainty. In addition, four nuisance parameters α_l centered at 0 with unit standard deviation are introduced to scale the four pull curves used to model the non-linearity uncertainty [16], and their contributions are added in quadrature to the χ^2 as penalty terms.

C. Statistical approaches

The framework described above supports fitting both Asimov datasets, which represent the nominal expectation without fluctuations, and pseudo-experiment (toy MC) datasets, which include statistical and systematic variations. The Asimov approach provides an estimate of the expected sensitivity from a single dataset, whereas the toy MC method employs 10,000 pseudo-datasets to extract distributions of best-fit values and uncertainties, thereby determining the achievable precision from the median. Both methods, using either a covariance matrix or pull terms as described in the previous subsection, are applied to the Asimov and toy MC datasets. The results are in excellent agreement, with deviations between the Asimov and toy MC approaches observed at lower exposures or reduced signal rates, as expected. The minor differences between the covariance and pull-term approaches are treated as a source of systematic uncertainty.

For the Asimov case, each input spectrum is scaled according to the expected number of events, based on the assumed experimental exposure and the rates provided in Table 3. These individual spectra are then summed to produce a single, non-fluctuated spectrum, with error bars reflecting realistic statistical uncertainties. It is worth noting that when using shapes generated from Monte Carlo simulations, the simulated statistics are significantly higher than the expected number of events.

For each toy MC dataset, the systematic uncertainties are varied by independently sampling each source from a Gaussian distribution with mean equal to the central expected value and standard deviation given by the corresponding uncertainty, avoiding over-constraints from highly correlated parameters. The toy MC approach enables estimating the probability that the geoneutrino signal cannot be identified and converges to the physical boundary at zero, which is particularly relevant at low exposures and small signal rates. This is illustrated for a 20 TNU geoneutrino signal and a 1 year exposure in Fig. 6 (a). We exclude from further analysis any such configurations where the probability of failing to identify the geoneutrino signal exceeds 0.27%, which corresponds to a 3σ confidence level. The remaining panels of Fig. 6 illustrate the procedure used to evaluate JUNO's precision in measuring geoneutrinos. This precision is quantified as the median of the distribution of individual fit uncertainties, defined as $\sigma_{N_{\rm geo}}/N_{\rm geo}$, with the corresponding uncertainty given by the ±34% confidence interval around the median. Note that these intervals are asymmetric due to the underlying asymmetry in the distribution of fit errors $\sigma_{N_{\rm geo}}$. The toy MC approach allows also to study correlations among spectral components, as illustrated in Fig. 7. The adopted method automatically takes such correlations into consideration.

D. Mantle discovery potential analysis strategy

This work also includes an assessment of JUNO's ability to distinguish the mantle signal from the lithospheric signal. We evaluated all three Bulk Silicate Earth (BSE) model types—Poor-H, Medium-H, and Rich-H—by injecting their respective signal strengths and thorium-to-uranium ratios (see Table 1). To comprehensively represent current lithospheric models, discussed in Section IV.A, we varied the lithospheric signal strength from 25 to 50 TNU and its associated uncertainty from 5% to 25%.

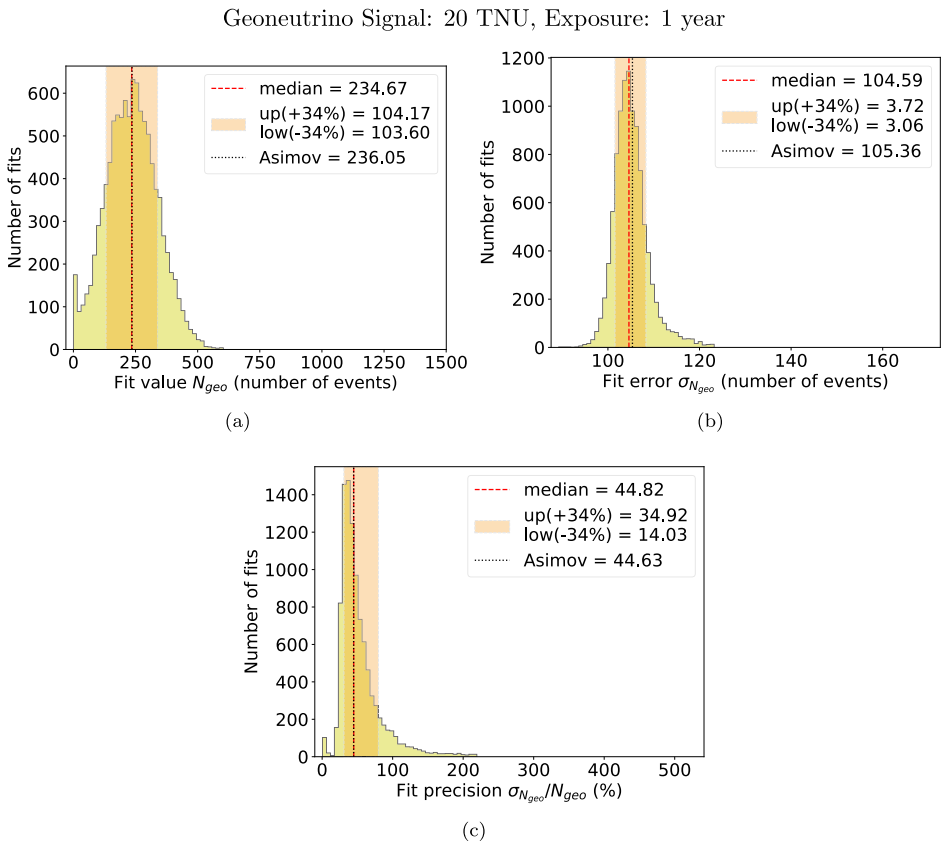


Fig. 6. (color online) Distributions of fit results from 10,000 toy MC pseudo-datasets are shown and compared to the Asimov approach results (dotted vertical lines) for 20 TNU geoneutrino signal and 1 year exposure. The dashed lines indicate the medians of the distributions, while the shaded vertical bands correspond to the ±34% confidence intervals. (a) Fitted number of geoneutrino events, $N_{\rm geo}$. A clear peak in $N_{\rm geo}$ converging to the physical boundary at zero is observed. (b) Corresponding fit uncertainty $\sigma_{N_{\rm geo}}$. (c) Relative precision, defined as $\sigma_{N_{\rm geo}}/N_{\rm geo}$, represents the JUNO sensitivity to measure geoneutrinos.

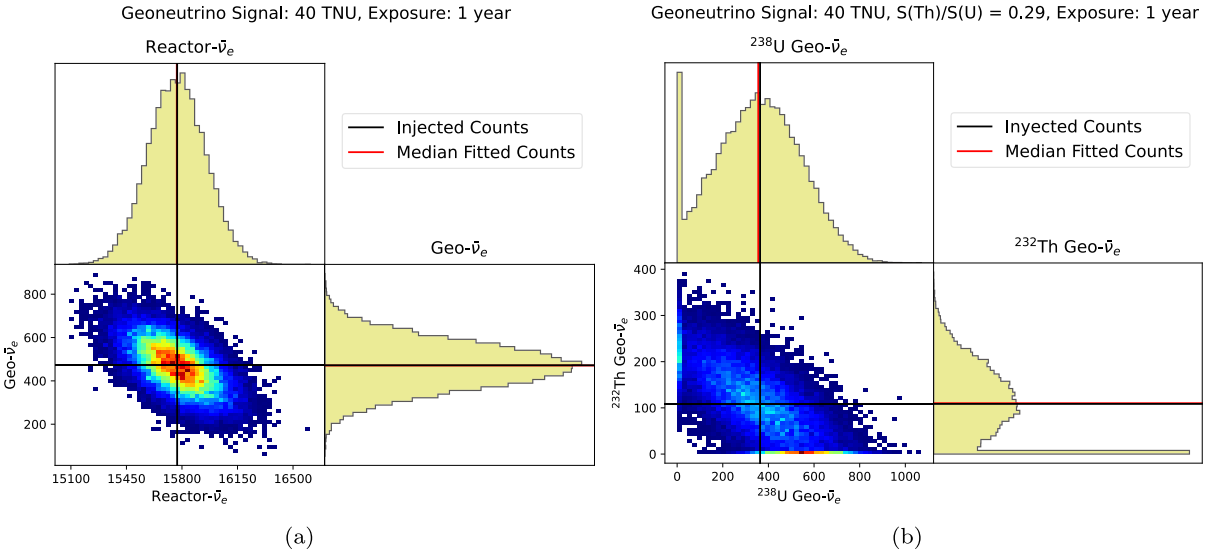


Fig. 7. (color online) Fit result distributions from 10,000 toy MC pseudo-datasets, showing spectral component correlations for one year of exposure and a 40 TNU geoneutrino signal. Left: anti-correlation between the geoneutrino component $N_{\rm geo}$ and the reactor antineutrino component $N_{\rm rea}$, assuming a fixed Th/U ratio for geoneutrinos at the chondritic value. Right: anti-correlation between the individual $N_{\rm U}$ and $N_{\rm Th}$ components.

For each set of mantle and lithospheric signal strengths, we generated two types of datasets, both including the lithospheric signal, but only one also incorporating the mantle contribution. These datasets were used to evaluate our ability to distinguish between the null hypothesis (no mantle signal) and the alternative hypothesis, in which the mantle signal is present. We tested the procedure using both Asimov and large-statistics toy MC datasets and found the resulting discovery potentials to be in good agreement. For computational reasons, the full scan was therefore performed using only the Asimov datasets.

Each dataset was fitted twice using the procedure described in Section VI.B. The only modification was that, instead of fitting the total geoneutrino signal $N_{\rm geo}$, we fitted the lithospheric signal $N_{\rm litho}$ and the mantle signal $N_{\rm mantle}$ separately. The lithospheric signal was constrained according to the assumed level of prior knowledge, while the mantle signal was either fixed to zero, yielding χ^2_0, or treated as a free parameter, yielding χ^2_1. We then define the test statistic $\Delta\chi^2 = \chi^2_0 - \chi^2_1$, with $\Delta\chi^2_0$ for the dataset without an injected mantle signal and $\Delta\chi^2_1$ for the dataset with the mantle signal. In the Asimov approach, $\Delta\chi^2_0 = 0$, since in the absence of statistical fluctuations, the data set without the mantle can be perfectly fit under both hypotheses, yielding $\chi^2_0 = \chi^2_1 = 0$. In the toy MC approach, $\Delta\chi^2_0$ was typically also close to zero, though always positive, as statistical fluctuations can mimic a mantle signal and reduce χ^2_1 relative to χ^2_0. In contrast, for datasets including a mantle contribution, the test statistic $\Delta\chi^2_1$ can attain large values, since the spectral fit is significantly worse when the mantle signal is omitted. In the Asimov approach, $\Delta\chi^2_1 = \chi^2_0$, since $\chi^2_1 = 0$. The discovery potential, expressed in units of σ, is thus defined as $\sqrt{\chi^2_0}$, obtained from fitting the dataset with an injected mantle signal under the null hypothesis, where the mantle contribution is set to zero.

Figure 8 illustrates the distributions of $\Delta\chi^2_0$ and $\Delta\chi^2_1$ for the Medium-H BSE model, based on simulated datasets corresponding to six years of exposure using the toy MC approach. The lithospheric signal is set to 35 TNU, with a 10% constraint applied during the fit. We define the discovery potential p-value as the probability that $\Delta\chi^2_0$ exceeds the median of the $\Delta\chi^2_1$ distribution, expressed by the filled orange area. To express the discovery potential in terms of significance, we convert the p-value to an equivalent number of standard deviations ($n\sigma$) assuming a normal distribution.

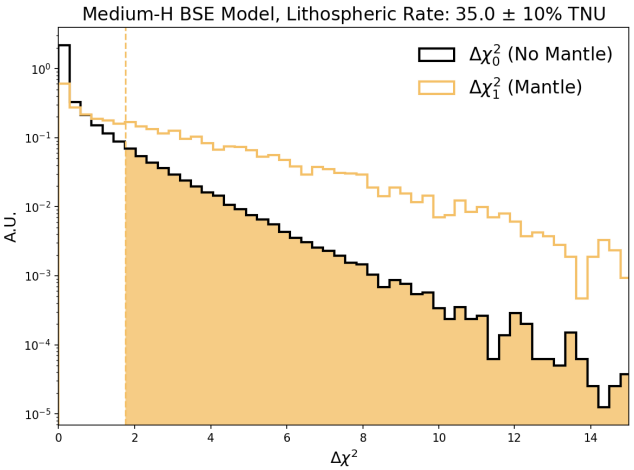


Fig. 8. (color online) Demonstration of JUNO's discovery potential for the mantle geoneutrino signal using six years of data with the toy MC approach. We present $\Delta\chi^2_0$ for datasets without an injected mantle signal (black solid line), alongside $\Delta\chi^2_1$ for datasets including mantle signals corresponding to the Medium-H BSE model (solid orange line). The vertical orange dashed line represents median of $\Delta\chi^2_1$ distribution. The discovery potential is defined as the p-value, e.g. the probability that $\Delta\chi^2_0$ exceeds the median of the $\Delta\chi^2_1$ distribution, represented by the orange filled area. The injected lithospheric signal is set to 35 TNU on which a constraint with 10% uncertainty is applied during the fit.

VII. RESULTS ON JUNO EXPECTED SENSITIVITY TO GEONEUTRINOS

The expected precision on the geoneutrino signal at JUNO depends strongly on both the integrated exposure and the true geoneutrino signal strength. In the following sections, we present sensitivity projections for exposures of up to 10 years, covering the range of geoneutrino signals predicted by different geological models as discussed earlier. Section VII.A focuses on the measurement of the total geoneutrino signal under the condition of a fixed thorium-to-uranium (Th/U) ratio in the fit, corresponding to the injected chondritic value. Section VII.B explores the case where the U and Th contributions are fitted independently. Finally, Section VII.C is dedicated to assessing JUNO's potential to detect the mantle geoneutrino signal as an excess above the constrained lithospheric contribution. All results were independently cross checked by different analyses groups and the eventual sub-dominant differences were treated as an additional systematic error.

A. Total geoneutrino signal with U and Th fixed ratio

The JUNO projected precision for measuring the total geoneutrino signal, assuming a fixed Th/U ratio in the fit, is shown in Fig. 9. Results are presented for exposures of 1, 3, 6, and 10 years, and for geoneutrino signal values ranging from 20 to 70 TNU, covering the full range of predictions from various geological models (indicated by the yellow area representing 1σ interval from Table 2). For each exposure and signal value, the central value is taken as the average between the two statistical ap-

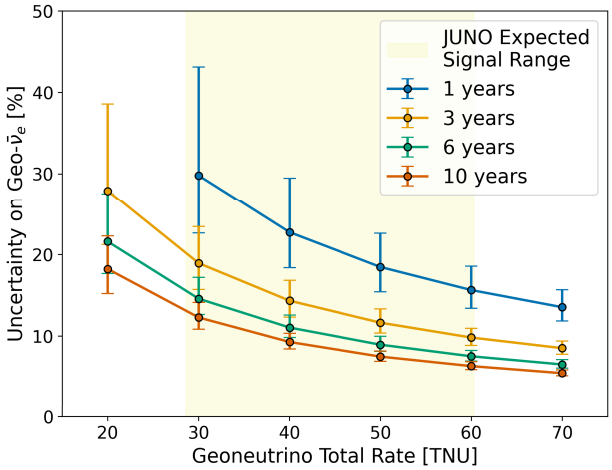


Fig. 9. (color online) Expected JUNO sensitivity to the total geoneutrino signal, assuming a fixed chondritic Th/U ratio, as a function of the total geoneutrino signal. The solid blue, orange, green, and red curves represent exposures of 1, 3, 6, and 10 years, respectively. The vertical yellow shaded area indicates the 1σ range from Table 2, encompassing the spread of different BSE models as well as various predictions for the lithospheric contribution.

proaches—Asimov and toy MC. The associated uncertainty corresponds to the ±34% confidence interval of the distribution of relative precisions obtained from 10,000 toy MC fits, as demonstrated in Fig. 6(c). These intervals are asymmetric, reflecting the inherently asymmetric nature of the fit uncertainties in individual toy MC realizations, as illustrated in Fig. 6(b). We present the estimated JUNO precision only for cases where the probability that the fitted signal differs from zero is sufficiently high, approximately corresponding to a discovery potential greater than 3σ. Therefore, the case shown in Fig. 6, where the peak at 0 fitted geoneutrino signal is clearly visible, is not represented in the results shown in Fig. 9.

For a low-signal scenario of approximately 30 TNU, corresponding to the lower edge of the 1σ band across various geological models, JUNO would achieve a precision of about 18%, comparable to existing geoneutrino measurements by Borexino and KamLAND, after roughly 3 to 6 years. For an intermediate signal of 40 TNU, falling well in the yellow band of expected geological predictions, the uncertainty improves more significantly: from $22.7^{+6.7}_{-4.3}$% after 1 year to $14.3^{+2.5}_{-2.0}$% at 3 years, $11.0^{+1.5}_{-1.2}$% at 6 years, and $9.3^{+1.1}_{-0.9}$% after 10 years. At the high end, assuming a total signal of 60–70 TNU, the uncertainty can be reduced further, reaching values as low as 5.4% in 10 years.

This level of precision will enable JUNO to distinguish between competing models of Earth's radiogenic heat production and to contribute substantially to our understanding of the Earth's internal composition.

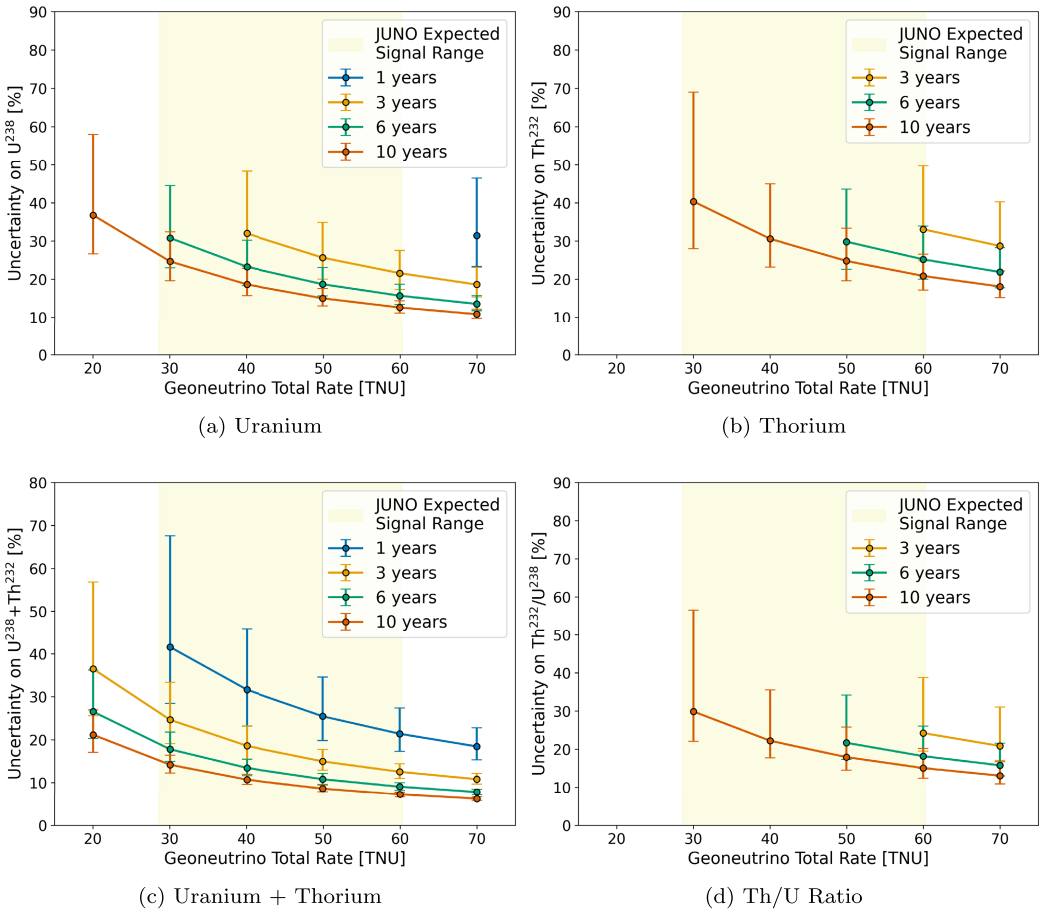
B. Uranium and thorium independent contributions

In this section, we present JUNO's projected sensitivity to the individual geoneutrino contributions from uranium (^{238}U) and thorium (^{232}Th), as well as their sum and ratio. Unlike the previous case in Section VII.A, where a fixed Th/U signal ratio was assumed, here we allow for independent variation of the uranium and thorium components in the fit, thereby enabling a more detailed geochemical interpretation of the geoneutrino signal.

Figure 10 shows the relative uncertainties for the uranium (a), thorium (b), combined (c), and the Th/U ratio (d), as functions of the total geoneutrino signal. Four different exposure scenarios—1, 3, 6, and 10 years—are considered. The construction of Fig. 10 follows the same methodology as Fig. 9. Points corresponding to fits with geoneutrino signals consistent with zero at less than 3σ significance were excluded, the central values and error bars represent the medians and ±34% quantiles of the relative uncertainty distributions, respectively. As we can see, distinguishing the uranium and thorium contributions requires large statistics, as their spectral differences mainly appear in the high-energy tail of the geoneutrino spectrum. The uranium spectrum extends up to 3.27 MeV and dominates the region above 2.25 MeV, whereas the thorium spectrum ends at 2.25 MeV. Consequently, the uranium component can be identified earlier, with a statistically significant measurement feasible after about 3–4 years of data taking. In contrast, the thorium signal is harder to extract, as its spectrum is largely degenerate with the low-energy portion of the uranium spectrum and contributes only about 20%–30% to the total geoneutrino rate. For a total geoneutrino signal of 40 TNU, JUNO is expected to achieve a precision of $23.3^{+7.0}_{-4.9}$% on the uranium component and $37.0^{+23.1}_{-10.6}$% on thorium after 6 years of exposure. After 10 years, these uncertainties further improve to $18.7^{+4.2}_{-2.9}$% and $30.60^{+14.41}_{-7.40}$%, respectively.

JUNO's exceptional event statistics thus offer a unique opportunity to disentangle uranium and thorium geoneutrino components with high statistical significance and to constrain the Th/U signal ratio. As shown in panel (d) of Fig. 10, this measurement can take up to 10 years, depending on the total geoneutrino signal. At 10 years and a 40 TNU signal, JUNO could measure the Th/U ratio with a precision $22.23^{+13.32}_{-4.51}$%, providing valuable constraints on the global distribution of HPEs and Earth formation processes.

The combined uncertainty on the sum of U and Th geoneutrinos remains lower than the individual components due to the partial compensation of anti-correlated uncertainties. This is demonstrated for total geoneutrino signal of 40 TNU at Fig. 11. For example, at 6 years, the total uncertainty on S(U+Th) is $13.4^{+2.0}_{-1.8}$%. For comparison, assuming a fixed Th/U ratio reduces the uncertainty to $11.0^{+1.5}_{-1.2}$% (see Section VII.A). While the impact of fitting U and Th separately on the total signal precision is



(a) Uranium (b) Thorium

(c) Uranium + Thorium (d) Th/U Ratio

Fig. 10. (color online) Expected JUNO sensitivity to geoneutrino signal from Uranium (a), Thorium (b), their combination (c), and the Th/U ratio (d) as a function of the total geoneutrino signal. The solid blue, orange, green, and red curves represent exposures of 1, 3, 6, and 10 years, respectively. The vertical yellow shaded area indicates the 1σ range from Table 2, encompassing the spread of different BSE models as well as various predictions for the lithospheric contribution.

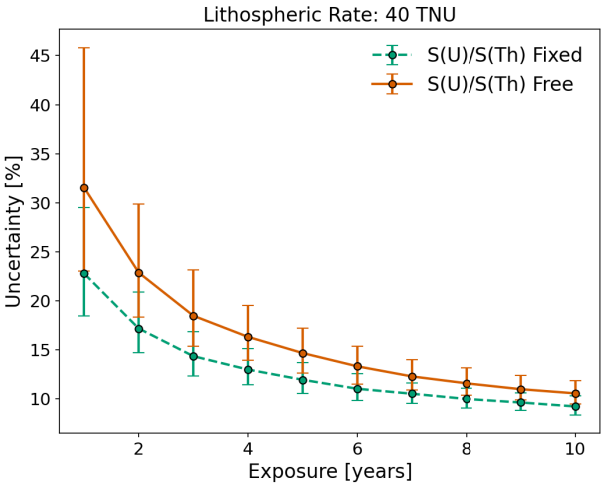


Fig. 11. (color online) Direct comparison of the expected JUNO sensitivity to the total geoneutrino signal (40 TNU) as a function of exposure, for two fitting approaches: one with the Th/U ratio fixed to the chondritic value (green dashed line), and the other with the Th/U ratio treated as a free parameter (orange solid line).

modest for longer exposures and higher signal levels, it becomes more relevant at lower exposures or in scenarios with reduced geoneutrino rates. For example, after just 1 year with the same 40 TNU signal, the uncertainty on S(U+Th) increases to $31.6^{+14.3}_{-8.5}$ when U and Th are left free to vary, compared to $22.7^{+6.7}_{-4.3}$ for a fixed Th/U fit.

These results highlight JUNO's potential to go beyond a total geoneutrino flux measurement and provide isotopic resolution critical for Earth science applications and directly test the Earth's Th/U ratio against model predictions.

C. Mantle signal

In this section we describe JUNO's discovery potential to identify the mantle geoneutrino contribution as an excess above the lithospheric prediction. Since the lithosphere provides the dominant share of the total signal and carries substantial uncertainties, the sensitivity to the mantle component depends strongly on both the assumed lithospheric signal strength and the precision with which it can be constrained.

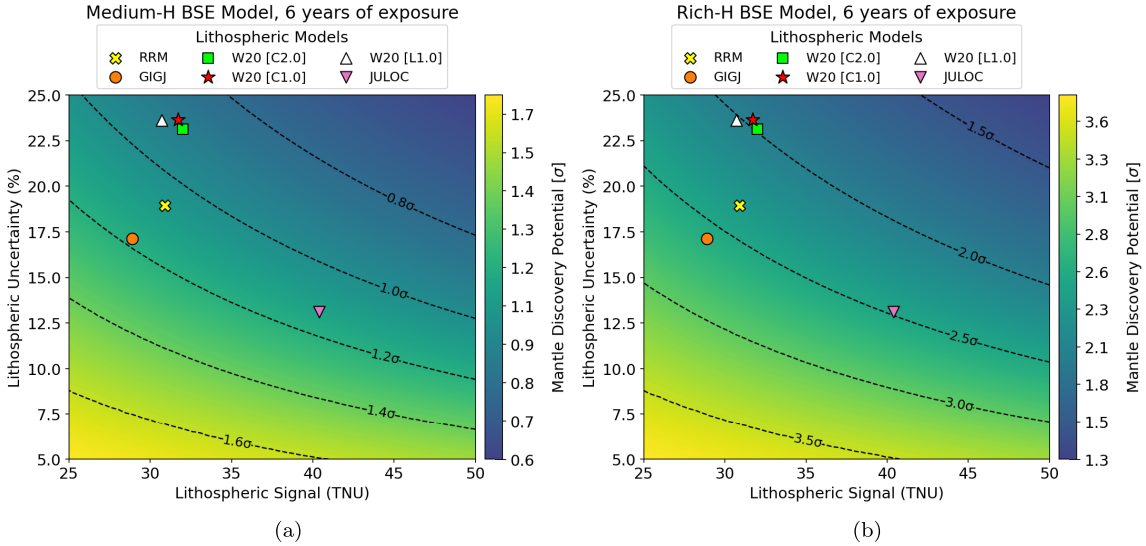


Fig. 12. (color online) Sensitivity to mantle geoneutrinos at JUNO with 6 years exposure for Medium-H (a) and Rich-H BSE (b) models. The color scale shows the statistical significance of mantle detection as a function of the assumed lithospheric signal strength (*X*-axis) and its uncertainty (*Y*-axis). Markers indicate benchmark lithospheric models as shown in Fig. 3.

Figure 12 illustrates JUNO's discovery potential for mantle geoneutrinos with 6 years of exposure, using the statistical method described in Section VI.D. The plot shows the dependence on the assumed lithospheric signal, varied between 25 and 50 TNU, and the precision of its constraint in the fit, varied between 5% and 25%. The lithospheric models from Fig. 12 are indicated with different markers to benchmark our scan. Three mantle radiogenic scenarios corresponding to different BSE models (Section IV.B) are considered.

For the Low-H BSE model, JUNO would not be able to identify the mantle signal, so this case is omitted from Fig. 12. For Medium-H BSE models, JUNO's sensitivity ranges between 1 and 1.6σ, depending on the lithospheric scenario assumed. A statistically significant detection of the mantle component becomes possible only for Rich-H BSE models with several years of data taking. In this scenario, a $\sim 3\sigma$ observation could be achieved after six years of exposure, assuming a lithospheric signal of 35 TNU constrained at the 10%–15% level. For the range of lithospheric models discussed above, the mantle signal discovery potential with 6 years of data lies between 2 and 2.5σ.

These results highlight the importance of improving crustal models around JUNO in order to reduce the dominant lithospheric uncertainty. Such progress, combined with JUNO's high statistics, will provide the opportunity to isolate the mantle geoneutrino flux at a continental margin site and to directly test Bulk Silicate Earth predictions.

VIII. CONCLUSIONS AND OUTLOOK

In this paper, we presented an updated evaluation of JUNO's sensitivity to geoneutrinos, building on an improved understanding of detector performance, updated background estimates, refined reactor neutrino flux predictions, and an enhanced analysis framework. Compared to previous estimates in Refs. [24, 48], this work includes a detailed treatment of uncertainties from both reactor and non-reactor backgrounds, allows oscillation parameters to float in the fit, and considers multiple fitting strategies. Sensitivity studies were performed using both Asimov datasets and large ensembles of toy Monte Carlo simulations.

Our sensitivity results span a broad range of signal strengths, enabling comparison with a wide variety of predictions from different geological models. From available models, the lithospheric contribution is estimated as $S_{\rm LS}(\text{U+Th}) = 32.3^{+8.6}_{-6.6}$ TNU. Within the Bulk Silicate Earth (BSE) framework, Poor-H, Medium-H, and Rich-H models predict total geoneutrino signals at JUNO of $36.0^{+9.6}_{-7.4}$, $41.0^{+9.5}_{-7.7}$, and $50.2^{+10.1}_{-8.5}$ TNU, respectively, defining the expected range of geoneutrino observations. JUNO's large 20 kton liquid scintillator target enables the detection of 0.92 to 1.95 geoneutrino events per day, surpassing the total statistics collected by all previous experiments (Borexino, KamLAND, SNO+) within a single year.

Despite the significant reactor neutrino background from the nearby (< 300 km) nuclear power plants producing 43.2 IBD events per day, JUNO will substantially advance our knowledge of the geoneutrino flux. For a benchmark signal of 40 TNU, JUNO can measure the total geoneutrino signal with a precision of about 11% after six years, assuming a fixed Th/U signal ratio of 0.29. If uranium and thorium are treated independently,

the precision reaches around 14%. Importantly, JUNO's sensitivity allows for the first experimental disentanglement of uranium and thorium components: in the Medium-H scenario, the Th/U ratio can be measured with a precision of about 22% after ten years, while in the Rich-H scenario independent determinations of uranium and thorium become feasible after roughly three years. These measurements will provide key insights into the Earth's differentiation and thermal evolution.

Detecting the mantle contribution remains challenging due to the dominant and uncertain lithospheric signal. The mantle discovery potential depends strongly on the mantle signal strength and the adopted BSE scenario: for Medium-H models, the statistical significance after six years is limited to ~ 1–1.6σ, whereas for Rich-H models JUNO could achieve a 3σ detection if the crustal contribution is constrained to within 15%. Given that the local crust around JUNO accounts for more than half of the lithospheric signal, improved geological and geophysical modeling in this region is essential to reduce uncertainties and enhance sensitivity to the mantle contribution.

In summary, JUNO's dataset will substantially refine the measurement of the geoneutrino flux and its composition, placing the strongest constraints to date on the Earth's radiogenic heat production and Bulk Silicate Earth models. An accurate characterization of the local crust will be important to maximize the interpretive power of the results. JUNO's data will establish a benchmark for future geoneutrino measurements and global combined analyses.

ACKNOWLEDGMENT

We are grateful for the ongoing cooperation from the China General Nuclear Power Group.

APPENDIX: GEONEUTRINO SIGNAL PREDICTION AT JUNO

Lithospheric contribution

The lithosphere is the rigid outer shell of the Earth extends from approximately 5–10 km in oceanic regions to 100–200 km in continental areas [68]. The lithosphere includes (i) the Earth's crust, which comprises the thin oceanic crust (<10 km) and the thick continental crust (20–70 km), and (ii) the Continental Lithospheric Mantle (CLM), which is the portion of the mantle underlying the continental crust located between the Moho and the Lithosphere-Asthenosphere boundary (Fig. 3). The abundances of HPEs in the lithosphere vary significantly, with the continental crust exhibiting values on the order of 1 μg/g for U, while the oceanic crust and CLM has lower concentrations on the order of 0.1 μg/g and 0.01 μg/g, respectively [68].

For detectors situated on the continental crust, such as JUNO, the geoneutrino signal is predominantly influenced by the lithosphere, with 40%−80% of the flux originating from this reservoir, emphasizing its crucial role in geoneutrino studies [68]. This dominance arises primarily from the Local Crust (LOC), the region within a few hundred kilometers of the detector, which constitutes the largest contribution due to the geoneutrino flux's dependence on the inverse square of the distance. To enhance modeling accuracy, the LOC is analyzed separately from the Rest Of the Crust (ROC) (Fig. 3), allowing for a more detailed and precise characterization of the lithospheric geoneutrino signal [69, 62, 47, 54].

For this study, the geoneutrino signals from the LOC, ROC, and CLM reported in previous works were analyzed. All models employ different methodologies and approaches with variations in the size and coordinates of the LOC but remain strongly correlated due to partially shared geophysical and geochemical inputs. Below, the key aspects of each model are presented, emphasizing the key aspects for the geoneutrino signal at JUNO.

The geoneutrino signals expected at JUNO and reported in [61] (Fig. 4), are calculated using the global Refined Reference Earth Model [68], hereafter RRM, which details HPEs' abundances and distribution together with their uncertainties. Crustal thickness and uncertainty are derived from three global models (CRUST 2.0 [18], CUB 2.0 [55], and GEMMA [49]) with crustal layer proportions, density, and elastic properties from CRUST 2.0 and sediment layer data from [38]. While the HPEs abundances in the sediments, oceanic crust, upper crust and CLM are assumed to be relatively homogenous based on compiled databases, the U and Th content in the deep continental crust is determined on the basis of felsic-to-mafic ratio, inferred from seismic velocities. The LOC is defined as a 6° × 4° region (20°–24° N, 109°–115° E) nearly centered on JUNO.

GIGJ (GOCE Inversion for Geoneutrinos at JUNO) [43] is a 3D numerical model (cellsize: 50×50×0.1 km) derived by inverting GOCE gravimetric data over a 6° × 4° region exactly centered at JUNO. The a priori model integrates deep seismic sounding profiles, receiver functions, teleseismic *P*-wave velocity models, and Moho depth maps, each utilized according to their accuracy and spatial resolution. The unitary geoneutrino signals calculated using the site-specific subdivision of the crust of GIGJ (Table 2 of [43]) combined with the HPE abundances from RRM, provided the geoneutrino signal of the LOC. To determine the total lithospheric signal, the contributions from the ROC and the CLM were added, both computed based on the RRM (Table A1).

Wipperfurth *et al*. [63] present reference models for lithospheric geoneutrino signals using geophysical information from various sources, including CRUST2.0 [18], CRUST1.0 [31], and LITHO1.0 [41]. The contribu-

Table A1. Summary of geoneutrino signal (S (U+Th)) contributions from the Local Crust (LOC), Rest of the Crust (ROC), and Continental Lithospheric Mantle (CLM) for the different models. The LOC area extension (longitude × latitude) is reported for each model.

Model	**LOC Area extension**	**S(U + Th) [TNU]**			**Reference**
	(Long x Lat)	LOC	ROC	CLM	
RRM	$6^\circ \times 4^\circ$	$16.4^{+3.0}_{-2.6}$	$11.7^{+2.3}_{-1.9}$	$2.1^{+2.9}_{-1.3}$	[61]
GIGJ	$6^\circ \times 4^\circ$	$14.4^{+2.5}_{-2.4}$	$11.7^{+2.2}_{-1.9}$	$2.1^{+2.9}_{-1.3}$	[43]
W20 [Crust_2.0]	$6^\circ \times 4^\circ$	$16.9^{+4.3}_{-3.4}$	$11.8^{+3.3}_{-2.6}$	$1.7^{+2.9}_{-1.1}$	[63]
W20 [Crust_1.0]	$6^\circ \times 4^\circ$	$16.7^{+4.4}_{-3.5}$	$11.7^{+3.3}_{-2.6}$	$1.7^{+2.9}_{-1.1}$	[63]
W20 [Lithos1.0]	$6^\circ \times 4^\circ$	$17.1^{+4.5}_{-3.6}$	$12.7^{+3.6}_{-2.8}$	$0.6^{+0.9}_{-0.4}$	[63]
JULOC	$10^\circ \times 10^\circ$	$28.5^{+4.5}_{-4.5}$	$9.8^{+1.7}_{-1.7}$	$2.1^{+2.9}_{-1.3}$	[41]

tions of the LOC (coincident with the extent defined by [61]), ROC, and CLM to the geoneutrino signal at JUNO are provided considering the three different geophysical models. The HPE abundances are derived using a strategy similar to the RRM, based on probability density functions of compressional wave velocity and SiO_2 abundance for the deep continental crust and on average global abundances for the remaining lithospheric reservoirs.

JULOC [47] is a 3D model of the LOC represented by the closest 10° × 10° crust surrounding the detector (17°–27° N, 107.5°–117.5° E). The geophysical inputs include a 3-D shear wave velocity model inverted from seismic ambient noise tomography. The crust is divided into upper, middle, and lower layers, with the upper crust further divided into a top layer of sedimentary rocks and granite intrusions, and a bottom layer of Precambrian basement rocks. The geochemical inputs are based on U and Th abundances from over 3000 rock samples in the region and are statistically evaluated for each crustal layer, with the uppermost layer having higher U and Th abundances. Besides the geoneutrino signal for the LOC, [47] reported also the signals produced by the ROC (modeled with CRUST 2.0 and compiled geochemical data) and by the CLM, inherited by [61] (Table A1).

The geoneutrino signal predicted by the JULOC model is significantly higher than those of the other models (Table A2). While most models report a lithospheric geoneutrino signal $S_{\rm LS}({\rm U+Th})$ with a central value in the range of 28.9 TNU to 32.0 TNU, with an average relative uncertainty of about 20%, JULOC stands out with a much larger signal of $S_{\rm LS}({\rm U+Th}) = 40.4$ TNU and a lower relative uncertainty (~ 10%) (Fig. 4). The ratios of S(Th)/S(U) remain consistent across all models, with values clustering around 0.30–0.31. This stability reflects the strong correlation between U and Th contributions and highlights the uniformity in the assumed Th/U abundance ratio across the models.

Note that each of the considered works, published between 2015 and 2020, adopt different oscillation parameters based on the available values at the time of the publication. Although subsequent updates to these parameters may introduce slight variations in the geoneutrino signal calculation, their impact on the average oscillation probability is small compared to the uncertainties arising from geological inputs and assumptions.

Since the six models used to estimate the geoneutrino signal share common features (e.g., global geophysical models, U and Th abundances in crustal layers), it is necessary to account for strong correlations when calculating a single central value and the corresponding uncer-

Table A2. Predicted geoneutrino signals (S(U+Th)) at JUNO and its components (S(U)) and (S(Th)) for the different lithospheric models together with the corresponding ratio S(Th)/S(U). The combined signal represents a statistically integrated result, incorporating contributions from all models. Uncertainties are reported as 1σ interval.

Model	S_{LS} (U) [TNU]	S_{LS} (Th) [TNU]	S_{LS} (U+ Th) [TNU]	S_{LS} (Th)/S_{LS} (U)
RRM	$23.2^{+5.9}_{-4.8}$	$7.3^{+2.4}_{-1.5}$	$30.9^{+6.5}_{-5.2}$	0.31
GIGJ	$22.0^{+5.4}_{-4.1}$	$6.6^{+1.7}_{-1.2}$	$28.9^{+5.5}_{-4.4}$	0.30
W20 [Crust 2.0]	$24.5^{+6.4}_{-5.1}$	$7.4^{+2.1}_{-1.7}$	$32.0^{+8.2}_{-6.6}$	0.30
W20 [Crust 1.0]	$24.2^{+6.5}_{-5.1}$	$7.4^{+2.2}_{-1.7}$	$31.7^{+8.4}_{-6.6}$	0.31
W20 [Litho 1.0]	$23.6^{+6.4}_{-5.0}$	$7.1^{+2.0}_{-1.6}$	$30.7^{+8.1}_{-6.4}$	0.30
JULOC	$30.3^{+4.9}_{-4.4}$	$9.2^{+1.7}_{-1.4}$	$40.4^{+5.6}_{-5.0}$	0.30
Combined	$24.7^{+6.7}_{-5.5}$	$7.5^{+2.2}_{-1.8}$	$32.3^{+8.6}_{-6.6}$	0.30

tainty for the expected lithospheric signal at JUNO. Specifically, 10^6 values were generated for each geoneutrino model based on its probability density function, representing the signal distributions predicted by the respective models. The generated samples were pooled into an aggregated dataset, from which the median and the 16^{th} and 84^{th} percentiles (defining the 1σ interval) were extracted.

Mantle contribution

Once the total U and Th content is fixed for a given BSE class, and the lithospheric U and Th abundances are determined ($H_{\text{LS}} = 6.9^{+1.6}_{-1.2}$ TW), [68]), the residual amounts of U and Th in the mantle are calculated in by subtracting the lithospheric contribution from the total BSE estimates (Table 29 of [30]). The mantle radiogenic heat obtained for each class (Table 1) reflects the assumptions regarding the Earth's primordial composition and the partitioning of HPEs.

The expected mantle geoneutrino signal for each BSE class is determined using the linear relation $S_{\text{M}}(\text{U}+\text{Th}) = \beta \cdot H_{\text{M}}(\text{U}+\text{Th})$, where β represents the proportionality coefficient that depends solely on the spatial distribution of uranium (U) and thorium (Th) in the mantle. The value of β ranges from $\beta_{\text{low}} = 0.75$ TNU/TW when HPEs are concentrated in a thin layer above the core-mantle boundary to $\beta_{\text{high}} = 0.98$ TNU/TW for a homogeneous mantle distribution; the average value is $\beta = 0.86$ TNU/TW [40, 30]. Using the radiogenic heat values $H_{\text{M}}(\text{U}+\text{Th})$ for the three BSE classes, the corresponding geoneutrino signals $S_{\text{M}}(\text{U}+\text{Th})$ can be plotted (Fig. A1). Specifically, the central value of the geoneutrino signal is determined by using the median $H_{\text{M}}(\text{U}+\text{Th})$ and applying the average β. The upper limit of uncertainty for $S_{\text{M}}(\text{U}+\text{Th})$ is obtained by increasing $H_{\text{M}}(\text{U}+\text{Th})$ by one standard deviation and applying β_{high}. Conversely, the lower uncertainty limit is calculated by decreasing $H_{\text{M}}(\text{U}+\text{Th})$ by one standard deviation and using β_{low} (Fig. A1). This method provides a comprehensive approach to estimate the expected geoneutrino signal ranges for different mantle compositions and distribution scenarios.

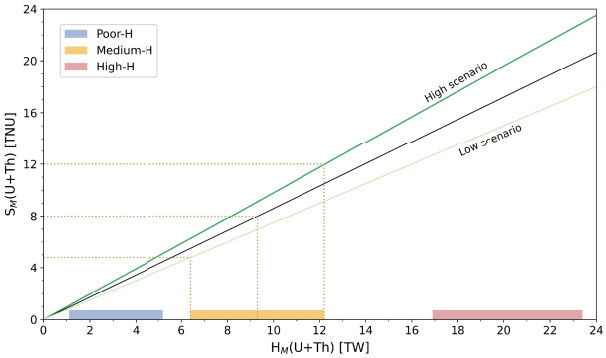


Fig. A1. (color online) Mantle geoneutrino signal (S_{M}(U+Th)) as a function of U and Th mantle radiogenic heat $H_{\text{M}}(\text{U}+\text{Th})$. The blue, yellow, and red bands on the X-axis correspond to the 68% coverage interval of the mantle radiogenic heat ($H_{\text{M}}(\text{U}+\text{Th})$) of Poor-H, Medium-H, and Rich-H models (Table 1), respectively. The area between the green lines denotes the full range allowed between a homogeneous mantle (high scenario, $\beta = 0.98$ TNU TW^{-1}) and a unique enriched layer just above the core-mantle boundary (low scenario, $\beta = 0.75$ TNU TW^{-1}); the inclined black line identifies the average coefficient ($\beta = 0.86$ TNU TW^{-1}). The dashed yellow line depicts, as an example, the method adopted to derive the central value of the $S_{\text{M}}(\text{U}+\text{Th})$ together with the upper and lower bounds for the Medium-H class.

The individual signal contributions of uranium $S_{\text{M}}(\text{U})$ and thorium $S_{\text{M}}(\text{Th})$ to the mantle geoneutrino signal for each BSE class are computed using the relation $S_{\text{M}}(\text{Th})/S_{\text{M}}(\text{U}) = 0.069 \times [M_{\text{Th}}/M_{\text{U}}]$ [40], where M_{Th} and M_{U} are the thorium and uranium mass in the mantle. By applying the mass ratios from Table 29 of [30] and the mantle geoneutrino signal $S_{\text{M}}(\text{U}+\text{Th})$, the individual signals $S_{\text{M}}(\text{U})$ and $S_{\text{M}}(\text{Th})$ can be derived together with their ratio $S_{\text{M}}(\text{Th})/S_{\text{M}}(\text{U})$, as it was shown in Table 1. Since the main uncertainties in the mantle signal arise from variations in the total U and Th content across different BSE classes and their spatial distribution within the mantle, the uncertainty in the $M_{\text{Th}}/M_{\text{U}}$ ratio is negligible in the overall error budget.

References

[1] A. Abusleme *et al.* (JUNO Collaboration), (2020), arXiv: 2005.08745

[2] A. Abusleme *et al.* (JUNO Collaboration), Eur. Phys. J. C **81**, 10 (2021)

[3] A. Abusleme *et al.* (JUNO Collaboration), NIM-A **988**, 164823 (2021)

[4] A. Abusleme *et al.*(JUNO Collaboration), JHEP **11**, 102 (2021)

[5] A. Abusleme *et al.* (JUNO Collaboration), JHEP **03**, 004 (2021)

[6] A. Abusleme *et al.*(JUNO Collaboration), JCAP **10**, 033 (2022)

[7] A. Abusleme *et al.* (JUNO Collaboration), Eur. Phys. J. C **82**(12), 1168 (2022).

[8] A. Abusleme *et al.* (JUNO Collaboration), Chin. Phys. C **46**(12), 123001 (2022)

[9] A. Abusleme *et al.* (JUNO Collaboration), Prog. Part. and Nucl. Phys. **123**, 103927 (2022)

[10] A. Abusleme *et al.* (JUNO Collaboration), Chin. Phys. C **47**, 113002 (2023)

[11] A. Abusleme *et al.* (JUNO collaboration), JCAP **10**, 022 (2023)

[12] A. Abusleme *et al.* (JUNO Collaboration), NIM-A **1057**, 168680 (2023)

[13] A. Abusleme *et al.* (JUNO Collaboration), Eur. Phys. J. Plus **139**(12), 1128 (2024)

[14] A. Abusleme *et al*. (JUNO collaboration), JCAP **2024**(01), 057 (2024)
[15] A. Abusleme *et al*. (JUNO Collaboration), Chin. Phys. C **49**, 013003 (2025)
[16] A. Abusleme *et al*.(JUNO Collaboration), Chin. Phys. C **49**(3), 033104 (2025)
[17] F. P. An *et al*. (Daya Bay Collaboration), Phys. Rev. Lett. **130**(16), 161802 (2023)
[18] C. Bassin, Eos Trans. AGU **81**, F897 (2000)
[19] https://doi.org/10.5281/zenodo.15157028
[20] E. Mendoza, D. Cano-Ott, P. Romojaro *et al*., Nucl. Instrum. Meth. A **960**, 163659 (2020)
[21] S. Enomoto, *Geoneutrino spectrum and luminosity*, online version
[22] M. Estienne. M. Fallot, A. Algora *et al*., Phys. Rev. Lett. **123**(2), 022502 (2019)
[23] G. Alimonti *et al*. (Borexino Collaboration), NIM-A **600**(3), 568 (2009)
[24] F. An *et al*. (JUNO Collaboration), J. Phys. G: Nucl. Part. Phys. **43**(3), 030401 (2016)
[25] F. P. An *et al*. (Daya Bay Collaboration), Phys. Rev. D **95**(7), 072006 (2017)
[26] F. P. An *et al*. (Daya Bay Collaboration), Chin. Phys. C **45**(7), 073001 (2021)
[27] F. P. An *et al*. (Daya Bay Collaboration), Chin. Phys. C **41**(1), 013002 (2017)
[28] G. Fiorentini, M. Lissia, and F. Mantovani, Phys. Rep. **453**, 117 (2007)
[29] G. Bellini, A. Ianni, L. Ludhova *et al*., Prog. Part. and Nucl. Phys. **73**, 1 (2013)
[30] G. Bellini, K. Inoue, F. Mantovani *et al*., La Rivista del Nuovo Cimento **45**(1), 1 (2021)
[31] G. Laske *et al*., *A 1-degree Global Model of Earth's Crust*, Geophysical Research Abstracts, 15, Abstract EGU2013-2658, (2013)
[32] Patrick Huber, Phys. Rev. C **84**, 024617 (2011) [Erratum: Phys. Rev. C **85**, 029901 (2012)
[33] IAEA, PRIS - power reactor information system 202x© IAEA, 2024. PRIS page
[34] J. Zhao *et al*. (JUNO Collaborations), Astrophys. J. **965**(2), 122 (2024)
[35] F. James and M. Roos, Comput. Phys. Commun. **10**(6), 343 (1975)
[36] K. Eguchi *et al*. (KamLAND Collaboration), Phys. Rev. Lett. **90**, 021802 (2003)
[37] J. Korenaga, Rev. Geophys. **46(2)**, RG2007 (2008)
[38] G. Laske and T. G. Masters, Eos Trans. AGU, **78**, F483 (1997)
[39] M. Abreu *et al*. (SNO+ Collaboration), (2025), arXiv: 2511.11856
[40] M. Agostini *et al*. (Borexino Collaboration), Phys. Rev. D **101**, 012009 (2020)
[41] M. E. Pasyanos, T. G. Masters, G. Laske *et al*., J. Geophys. Res. **119**(3), 2153 (2014)
[42] M. Javoy, E. Kaminski, F. Guyot *et al*., Earth Planet. Sci. Lett. **293**(3), 259 (2010)
[43] M. Reguzzoni, L. Rossi, M. Baldoncini *et al*., J. Geophys. Res. Solid Earth **124**(4), 4231 (2019)
[44] W. F. McDonough and S. Sun, Chem. Geol. **120**(3), 223 (1995)
[45] W. F. McDonough, O. Šrámek, and S. A. Wipperfurth, Geochem. Geophys. Geosyst. **21**, e2019GC008865 (2020)
[46] W. F. McDonough, *The Composition of the Lower Mantle and Core*, (2016), p. 143
[47] R. Gao, Z. Li, R. Han *et al*., Phys. Earth Planet. Interiors **299**, 106409 (2020)
[48] R. Han, Y. F. Li, L. Zhan *et al*., Chin. Phys. C **40**(3), 033003 (2016)
[49] M. Reguzzoni and D. Sampietro, Int. J. Appl. Earth Obs. Geoinf.**35**, 31 (2015)
[50] S. Abe *et al*. (KamLAND Collaboration), Geophys. Res. Lett.**49**, e2022GL099566 (2022)
[51] S. C. Albanese *et al*. (SNO+ Collaboration), JINST **16**, P08059 (2021)
[52] S. Navas *et al*.(Particle Data Group), Phys. Rev. D **110**(3), 030001 (2024)
[53] S. Wang, D. M. Xia, X. Zhang *et al*., Phys. Rev. D **103**(4), 043010 (2021)
[54] L. G. Sammon, W. F. McDonough, and W. D. Mooney, J. Geophys. Res. Solid Earth **127**(8), (2022)
[55] N. M. Shapiro and M. H. Ritzwoller, Geophys. J. Int. **151**, 88 (2002)
[56] A. Strumia and F. Vissani, Phys. Lett. B **564**(1), 42 (2003)
[57] T. A. Mueller, D. Lhuillier, M. Fallot *et al*, Phys. Rev. C **83**, 054615 (2011)
[58] T. Adam *et al*. (JUNO Collaboration), Eur. Phys. J. C **85**(9), 1080 (2025)
[59] D. Turcotte and G. Schubert, *Geodynamics*, (Cambridge University Press, 2018)
[60] V. Albanese *et al*. (SNO+ Collaboration), Phys. Rev. Lett. **135**, 121801 (2025)
[61] V. Strati *et al*., Prog. Earth Planet. Sci.**2**(1), (2015)
[62] V. Strati, S. A. Wipperfurth, M. Baldoncini *et al*., Geochem. Geophys. Geosyst. **18**(2), 4326 (2017)
[63] S. A. Wipperfurth, O. Šrámek, and W. F. McDonough, J. Geophys. Res. **125**(2), e2019JB018473 (2020)
[64] S. A. Wipperfurth, M. Guo, Ondřej Šrámek *et al*., Earth Planet. Sci. Lett.**498**, 196 (2018)
[65] B. J. Wood, M. J. Walter, and J. Wade, Nature, **441**(7095), 825 (2006)
[66] X. B. Ma, W. L. Zhong, L. Z. Wang *et al*., Phys. Rev. C **88**, 014605 (2013)
[67] X. Ji, W. Gu, X. Qian *et al*., Nucl. Instrum. Meth. A **961**, 163677 (2020)
[68] Y. Huang, V. Chubakov, F. Mantovani *et al*., Geochem. Geophys. Geosyst. **14**(6), 2003 (2013)
[69] Y. Huang, V. Strati, F. Mantovani *et al*., Geochem. Geophys. Geosyst. **15**(10), 3925 (2014)